Review

Samim Sardar and Samir Kumar Pal*

Ultrafast photoinduced carrier dynamics at ZnO nanohybrid interfaces for light-harvesting applications

DOI 10.1515/ntrev-2015-0053
Received October 1, 2015; accepted November 30, 2015; previously published online January 7, 2016

Abstract: The use of nanoscale materials for efficient solar light harvesting has attracted immense attention in the recent time in order to address the energy and environmental issues. Among them, semiconductor materials such as ZnO have been widely used in the field of photocatalysis and dye-sensitized solar cells (DSSC). However, due to limited visible-light activity and low photo-conversion efficiency, ZnO needs to be modified to design heterostructures with efficient charge separation. Several strategies have been made to modify the wide-bandgap semiconductors including narrow-bandgap semiconductor coupling, noble metal deposition, conducting polymer sensitization and organic dye sensitization. However, the activity of such heterogeneous systems critically depends on the charge dynamics across the involved nanostructured interface. The present review is an effort to unravel the ultrafast dynamical processes across the interface of heterostructures to enhance the solar light-harvesting efficiency. Here, we have discussed few of our selected results covering the different modification strategies of the ZnO nanostructures. The special emphasis has been given to the correlation between the ultrafast processes at the interface and their implications in the light-harvesting applications. The detailed spectroscopic investigations revealing electronic pathways for light harvesting will be helpful in designing future solar devices.

***Corresponding author: Samir Kumar Pal,** Department of Chemical, Biological and Macromolecular Sciences, S. N. Bose National Centre for Basic Sciences, Block JD, Sector III, Salt Lake City, Kolkata 700 098, India, e-mail: skpal@bose.res.in
Samim Sardar: Department of Chemical, Biological and Macromolecular Sciences, S. N. Bose National Centre for Basic Sciences, Block JD, Sector III, Salt Lake City, Kolkata 700 098, India

Keywords: Förster resonance energy transfer (FRET); interfacial carrier dynamics; light-harvesting heterostructures; UV and visible-light photocatalysis; zinc oxide.

1 Introduction

The efficient conversion of solar photons into electricity and chemical energy via cost-effective solar devices is one of the most important scientific challenges in the recent time. The solar energy conversion technology has shown hope to meet the rising energy demand as well as finding potential solutions for environmental pollution issues [1–3]. Semiconductor nanostructure materials such as TiO_2, ZnO have been widely used in waste water purification and solar energy conversion [4–9]. However, the large bandgap of TiO_2 (~3.2 eV) and ZnO (~3.37 eV) requires excitation only at wavelengths <390 nm [10, 11]. In this respect, the popular TiO_2, ZnO can only utilize ~5% of the incoming solar energy, thus, restricting its practical applications as efficient solar light harvester. The key to the efficient solar energy conversion is the development of high-performance functional materials, which has well matched photo absorption with the solar spectrum and an efficient photoexcited charge separation to prevent electron-hole recombination. Many efforts have been made to trigger the optical response of the wide bandgap semiconductor into the visible region by metal-ion doping [12], non-metal doping [13, 14], noble metal deposition [15, 16], narrow-bandgap semiconductor coupling [17–20], conducting polymer sensitization [21, 22], and dye sensitization [23–28]. The formation of organic-inorganic and inorganic-inorganic light-harvesting assemblies (LHAs) allows both a broader range of solar light absorption and efficient charge separation. However, the activity of such heterogeneous systems critically depends on the charge dynamics across the involved nanostructured interface [29].

LHAs used in photocatalysis (PC) and dye-sensitized solar cells (DSSC) are related to ultrafast excited state

charge transfer across the interface [30, 31]. Thus, a precise knowledge of excited state charge transfer across oxide surfaces is important to fully understand the microscopic mechanism related to technologically important processes of PC and DSSC, both of which, indeed, have strong social impact. In this direction, we have recently explored the ultrafast photoinduced charge separation and charge recombination processes at the semiconductor-semiconductor (PbS-ZnO) interface for efficient solar light harvesting [20]. The PbS-ZnO LHAs lead to efficient photovoltaics but their photocatalytic properties remain poor. Kamat and coworkers [32] show photoinduced electron transfer from CdSe quantum dots (QDs) of different sizes to three unique metal oxides (TiO_2, ZnO, and SnO_2) and suggest that, in addition to electron transfer at the QD-metal oxide interface, other loss mechanisms play key roles in the determination of overall device efficiency.

In order to sensitize the oxides in the visible light, sensitization with visible light-absorbing dyes is a prevalent solution. A considerable research effort in this direction stems from the desire to make cost-effective and environment-compatible dye-sensitized nanostructure-based solar light-harvesting devices [33, 34]. The synthesis and purification of the best-performing ruthenium-based dyes for the solar light-harvesting devices are expensive [35]. In the context of cost and biocompatibility, porphyrin-based solar devices are gaining a great interest in the contemporary literature [36–40]. In one of our recent studies, hematoporphyrin-sensitized ZnO nanorods exhibit twin applications in efficient visible light photocatalysis and DSSC [23]. The incorporation of metal ions in the central cavity of porphyrin in the proximity of host semiconductor for efficient decontamination of drinking water is a subject of several recent reports [41–43]. Tuning the photo response [44], stability of the dyes upon metalation [45] and efficiency of photo injected electron [46] are studied in a series of reports [47]. In one of our recent studies, we have investigated the critical role of central metal ions (Fe^{3+}/Fe^{2+}) incorporated in hematoporphyrin-TiO_2 nanohybrid in interfacial carrier dynamics and its implications in solar light harvesting [24]. We have also explored the role of metal ions, specifically, iron (III) and copper (II) in the test water with a model contaminant, methylene blue (MB) and rationalized our observations from femtosecond to picosecond resolved electronic spectroscopic studies [27].

One of the most interesting ways to make LHAs in the recent literature is amalgamation of semiconductor nanocrystals and polymers for the development of multifunctional materials that demonstrate superior electrical, optical, and mechanical properties [48–52]. Thus, incorporation of semiconductor nanocrystals into conjugated polymers can sensitize the semiconductor nanocrystals for renewable energy applications such as bulk heterojunction-type photovoltaics and photocatalysis [53–58]. A series of LHAs based on heterojunctions such as TiO_2-PANI, TiO_2-P3HT has been studied for the harvesting of visible light [59–63]. There is a common consensus that heterojunctions facilitate the migration of photoexcited electrons and holes across the interfaces to enhance charge separation. However, very few direct experimental evidences or spectroscopic observations have been explored to establish the charge transfer mechanism at the heterostructure interface. In a recent study, we have explored the charge transfer mechanism in a heterostructure based on poly(diphenylbutadiyne) (PDPB) nanofibers [64] and ZnO nanoparticles (NPs) by using the steady state and picosecond-resolved photoluminescence studies [22].

In this article, we will review the work at S N Bose Centre on the ultrafast dynamical processes across the interface of heterostructures to enhance the solar light-harvesting efficiency. Here, we will discuss few of our selected results covering the different modification strategies of the ZnO nanostructures. A significant number of research articles are available on the sensitization of semiconductors for solar light-harvesting devices. A comprehensive picture of most of the published works is not the motive of the present review; rather, we will elaborate four specific types of heterogeneous interfaces of ZnO NPs, namely, with other narrow bandgap semiconductors (quantum dots), noble metal NPs, organic dyes, and conducting polymers. Our main aim will be to correlate between the ultrafast processes at the interface and their implications in the light-harvesting applications. We will not discuss related works from this laboratory, which focused on other aspects of ultrafast dynamical studies related to photovoltaic applications.

2 Ultrafast dynamics at semiconductor-semiconductor interface

2.1 Interfacial dynamics of PbS-ZnO light-harvesting assemblies

In order to understand the key ultrafast processes associated at the interface between semiconductor-semiconductor heterostructure, we demonstrate our studies on the interfacial carrier dynamics in PbS-ZnO LHAs [20]. As

both the parent materials ZnO and PbS have their intrinsic photoluminescence (PL) because of their defect states and bandgap emission, respectively, steady-state spectroscopic studies on the LHA have been employed for the interfacial charge/energy migration.

As shown in Figure 1, the room temperature PL spectrum of ZnO NP is comprised of two emission bands upon excitation at 300 nm. The narrow UV band centered at 363 nm is due to the exciton recombination, and the other one is a broad emission in blue green region, which is composed of two bands, one arises from doubly charged vacancy center (Vo^{++}) located at 555 nm (P_2), and the other arises from singly charged vacancy center (Vo^{+}) located at 500 nm (P_1) [65, 66]. For PbS-ZnO LHAs, there is a considerable decrease in the intensity of both the emission peaks compared to the bare ZnO NPs. Herein, we propose Förster resonance energy transfer (FRET) [67, 68] from the donor ZnO NPs to the acceptor PbS QDs in PbS-ZnO LHAs. The spectral overlap of the defect-mediated PL band of ZnO NPs with that of the PbS absorption is shown in Figure 1A, inset. The fluorescence decay of bare ZnO NPs and PbS-ZnO LHAs was obtained upon excitation of 375 nm laser and monitored at 500 nm and 555 nm (Figure 1B and C, respectively). The faster average excited state lifetime of the PbS-ZnO LHAs with respect to that of the ZnO NPs is clearly observed. The details of the spectroscopic parameters and the fitting parameters of the fluorescence decays are tabulated in Table 1. From FRET

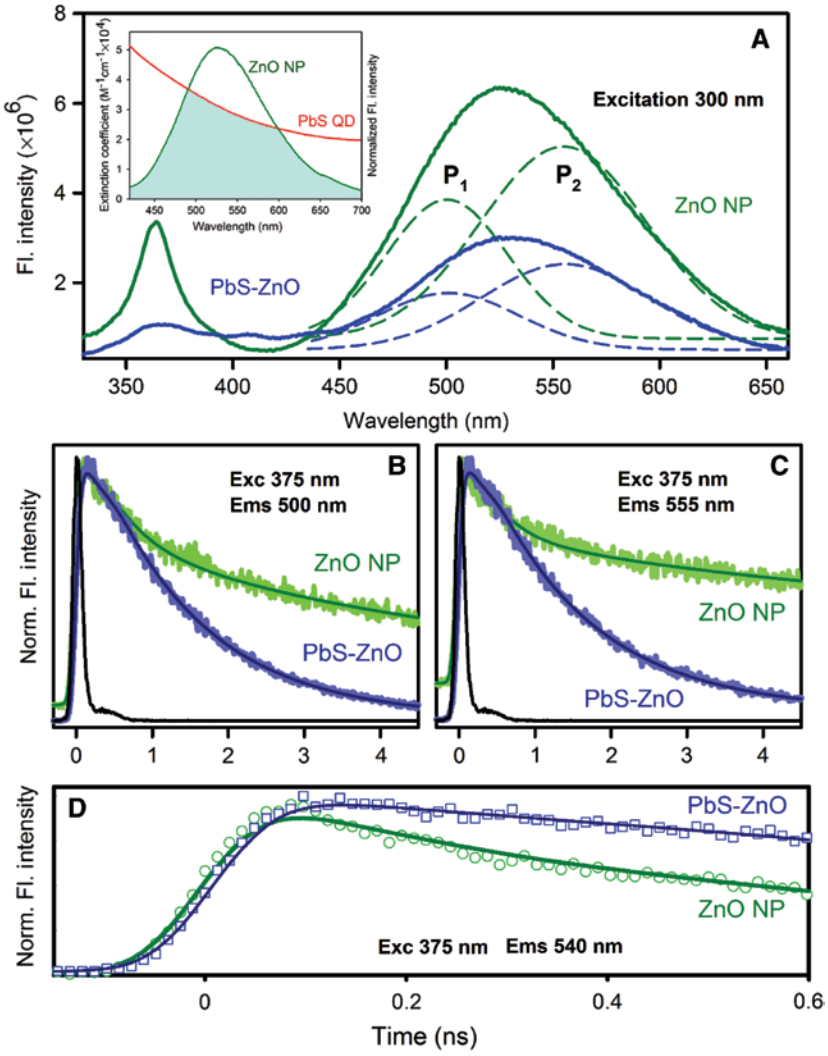

Figure 1: (A) Room temperature PL spectra of ZnO NPs (dark green) and PbS-ZnO LHAs (blue) are shown. The excitation wavelength was at 300 nm. The broad emission band is composed of two components, P_1 (500 nm) and P_2 (555 nm). The inset shows the overlap of ZnO NP emission and PbS QD absorption. The picosecond-resolved fluorescence transients of ZnO NPs (excitation at 375 nm) in the absence (dark green) and in the presence of PbS QDs (blue) collected at (B) 500 nm, (C) 555 nm, and (D) 540 nm (shorter time window) are shown. Reprinted with permission from Ref. [20] Copyright 2015, Elsevier B.V.

Table 1: Dynamics of picosecond-resolved luminescence transients of ZnO NP, PbS-ZnO LHA, and PbS QD.[a]

Sample	Excitation wavelength (nm)	Detection wavelength (nm)	τ_1 (ns)	τ_2 (ns)	τ_3 (ns)	τ_{avg} (ns)
ZnO NP	375	500	0.46±0.03 (43.8%)	4.52±0.05 (41.6%)	37.39±0.52 (14.6%)	7.55±0.09
PbS-ZnO LHA	375	500	1.30±0.05 (95.5%)	3.46±0.24 (4.5%)		1.39±0.03
ZnO NP	375	555	0.37±0.03 (46.2%)	5.07±0.12 (25%)	44.93±0.37 (28.8%)	14.38±0.14
PbS-ZnO LHA	375	555	1.32±0.05 (94.3%)	5.22±0.37 (4.5%)	42.29±2.76 (1.2%)	1.98±0.06
ZnO NP	375	540	0.38±0.03 (75.3%)	3.36±0.07 (17.2%)	38.64±0.69 (7.5%)	3.76±0.07
PbS-ZnO LHA	375	540	1.31±0.03 (92.8%)	4.79±0.51 (5.1%)	45.95±2.70 (2.1%)	2.42±0.12
PbS QD	375	820	1.17±0.05 (91%)	13.21±0.76 (9%)		2.25±0.08
PbS-ZnO LHA	375	820	1.41±0.05 (100%)			1.41±0.03
PbS QD	510	820	130.35±3.54 (100%)			130.35±3.54
PbS-ZnO LHA	510	820	0.04±0.03 (99.33%)	138.34±8.71 (0.66%)		0.95±0.06

[a]Numbers in the parentheses indicate relative weightages.

calculations, the distance between the donor and acceptor are determined to be 1.71 nm and 1.61 nm for P_1 and P_2 states, respectively. The energy transfer efficiency is calculated to be 81.6% and 86.3% from the P_1 and P_2 states, respectively. The observation is in agreement with the reported literature that the P_2 state is in the proximity of the NP surface [69, 70]. Further confirmation of nonradiative energy transfer from the ZnO NPs (donor) to the associated PbS QDs (acceptor) is evident from the emission characteristics of the acceptor as shown in Figure 2. The excitation spectrum of the LHAs at the detection wavelength of 820 nm as shown in Figure 2A clearly reveals a maximum at 360 nm, which is close to the absorption maximum of the ZnO NPs. In the case of FRET, it is expected that emission transient from the acceptor shows buildup in the timescale comparable to the decay of the energy donor [71]. As shown in Figure 2B, the emission transient of the acceptor PbS QDs reveal no apparent rise component. However, the shorter component of the lifetime of acceptor PbS QDs is significantly retarded in PbS-ZnO LHAs as shown in Table 1 revealing an intrinsic buildup in the excited state due to FRET. We have estimated the buildup rate following reported procedure [32] and found to be 1.45×10^7 s^{-1}, which is close to the FRET rate from donor ZnO NPs to acceptor PbS QDs (1.47×10^7 s^{-1}). As shown in Figure 2B, the overall quenching of the emission (steady state and transient) of PbS QDs in the LHAs clearly indicates that other nonradiative excited state events are associated following the energy transfer from the donor ZnO NPs. In order to investigate the nonradiative pathway of PbS QDs in the LHAs upon excitation, we have excited the nanocomposite at 510 nm and followed the steady and time-resolved emission as shown in Figure 3. The quenching of the emission of the PbS QDs in the LHAs clearly reveals ultrafast (Table 1) electron transfer from the excited QDs to the CB of ZnO NPs through the nonradiative pathway [72, 73]. Plass et al.

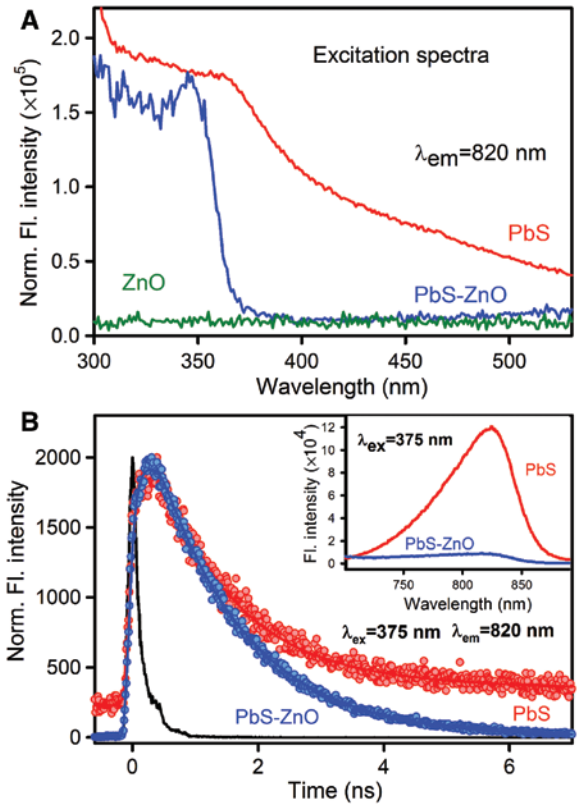

Figure 2: (A) Excitation spectra of ZnO NPs (dark green), PbS QDs (red) and PbS-ZnO LHAs (blue) monitored at 820 nm. (B) The picosecond-resolved fluorescence transients of PbS QDs (excitation at 375 nm) in the absence (red) and in the presence of ZnO NPs (blue) collected at 820 nm. The inset shows the room temperature PL spectra of PbS QDs (red) and PbS-ZnO LHAs (blue) upon excitation at 375 nm. Reprinted with permission from Ref. [20] Copyright 2015, Elsevier B.V.

[74] have investigated the electron transfer in a solar cell structure made by *in situ* growth of PbS QDs in a porous TiO_2 film, where initial charge separation occurs in 1 ps

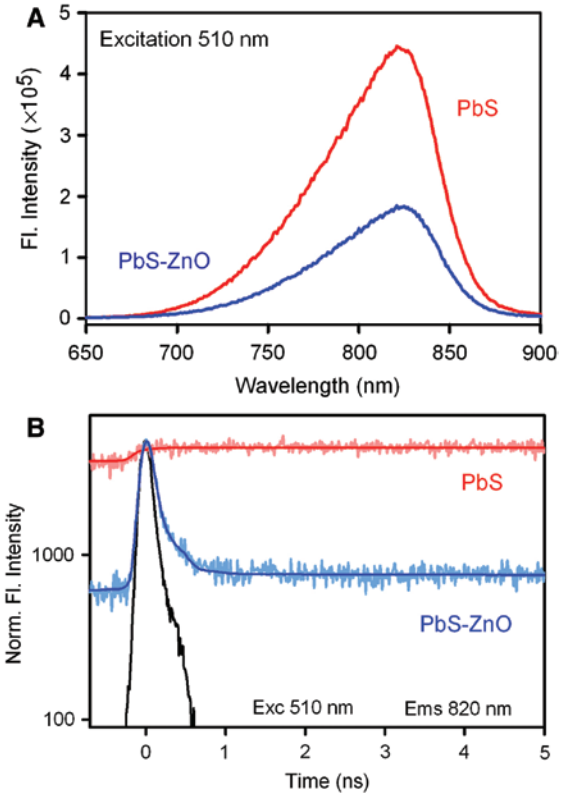

Figure 3: (A) Room temperature PL spectra (excitation wavelength was at 510 nm) of PbS QDs (red) and PbS-ZnO LHAs (blue) are shown. (B) Fluorescence decay profiles of PbS QDs in the absence (red) and presence of ZnO NPs (blue) upon excitation at 510 nm and monitored at 823 nm. Reprinted with permission from Ref. [20] Copyright 2015, Elsevier B.V.

due to the electron trapping in PbS QD followed by electron injection into the conduction band (CB) of TiO_2 having a time constant of 20 ps.

Table 1 reveals that the shorter component of the decay of bare ZnO NPs (0.46 ns and 0.37 ns for the P_1 and P_2 states, respectively) increases upon attaching to the PbS QDs (1.30 ns and 1.32 ns, respectively). The lengthening of the faster relaxation times from the P_1 and P_2 states confirms the following two phenomena. First, the quenching due to FRET is not operative in the timescale of ~400 ps. Second, the recombination processes in the ZnO defect states are heavily retarded in the proximity of PbS QDs as clearly shown in Figure 1D. The retardation of the recombination may be attributed to the quenching of the photoexcited holes of ZnO NPs by the PbS QDs. In our case, the photo-generated hole in the valence band of the ZnO NPs is proposed to be quenched by an electron from the valence band of PbS QDs, which is expected to be recovered from the electron in the CB/P_1 state of the ZnO NPs (lower panel of Figure 5).

In order to maximize the device efficiency, better understanding of mechanistic details of energy transfer processes is necessary. Eichberger et al. have shown that FRET in a multichromophoric organic sensitizer accommodating the separately linked donor and acceptor moieties attached to the ZnO nanorods reveal improved efficiency in DSSC [75]. Kamat et al. have unraveled that energy transfer through both long-range dipole-based FRET and short-range Dexter energy transfer (DET) mechanisms occurred between CdSe QDs linked to a red-infrared-absorbing squaraine dye [76]. The hybrid solar cells with squaraine dye as a linker between CdSe QD and TiO_2 exhibited power conversion efficiency of 3.65%. Transient absorption spectroscopy measurements reveal the energy transfer between excited CdSe QD and SQSH (rate constant of 6.7×10^{10} s^{-1}) and interfacial electron transfer between excited SQSH and TiO_2 (rate constant of 1.2×10^{11} s^{-1}) [77]. Thus, synergistic combination of electron and energy transfer processes provides new opportunities to harvest light from a different region of the solar spectrum, which eventually increases the efficiency of the device. In one of the previous publications from our group, the semiconductor ZnO NPs were found to transfer the excited state energy to sensitizing dye N719 at the surface of the NPs. The observed energy transfer in the presence of high-energy photons leads to a significant increase in the short circuit current in ZnO-based DSSC leading to more than 50% increased energy conversion efficiency [78].

2.2 Implications of interfacial dynamics of PbS-ZnO in light-harvesting applications

In order to investigate the interfacial charge transfer dynamics in photocatalysis application, we have probed the MB reduction in the presence of the LHA in aqueous solution. For the preferential excitation, we have used 475 nm high-pass (HP) optical filter placed on a home-made UV bath (8W) before the sample. The results for the photoreduction of MB are shown in Figure 4A. The photoreduction of MB implies the generation of the colorless photoproduct Leuco-Methylene Blue (LMB). The maximum photoreduction is observed in the presence of ZnO NPs under UV irradiation, while using a 475-HP optical filter, no photoreduction of MB is observed. This is obvious because ZnO being a wide-bandgap (3.37 eV) semiconductor, the bandgap excitation occurs only at wavelengths less than 380 nm. However, ZnO NPs in the proximity of PbS QDs in the LHAs show inefficient MB photoreduction both in the presence and absence of the

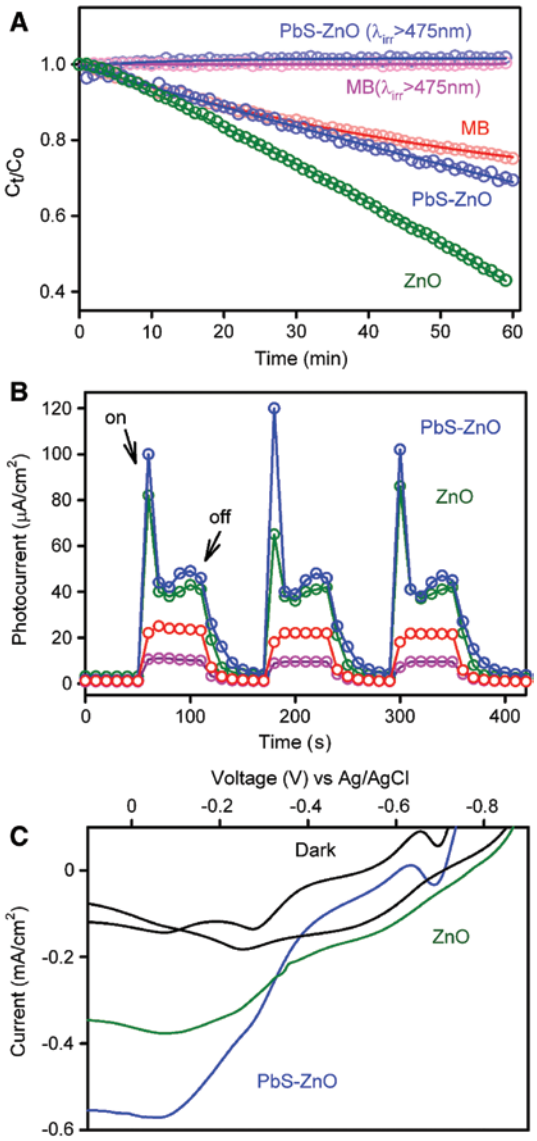

Figure 4: (A) Photocatalytic degradation of MB in the presence of ZnO NPs (green) and PbS-ZnO LHA (blue) and control (red and pink) under different irradiation conditions (the optical filters used for the desired irradiation are indicated in parentheses). (B) Photocurrent response of PbS-ZnO LHA (blue) and ZnO (green) under 100 mW cm^{-2} incident power irradiation and PbS-ZnO (red) and ZnO (pink) under visible light irradiation (using 400 nm filter) without any bias voltage. (C) Photocurrent-voltage (I–V) characteristics of PbS-ZnO LHA (blue) and ZnO (green) under 100 mW cm^{-2} incident power irradiation. Reprinted with permission from Ref. [20] Copyright 2015, Elsevier B.V.

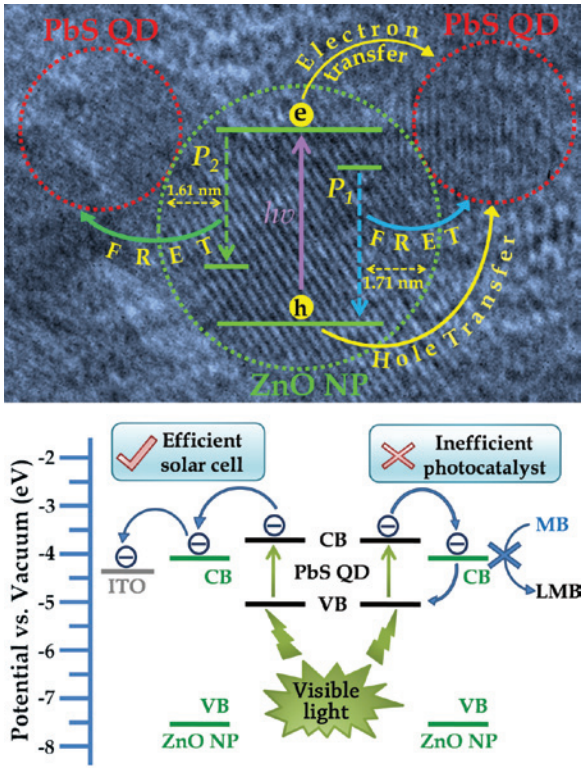

Figure 5: Schematic presentation of the interfacial carrier dynamics in PbS-ZnO LHAs (Upper panel). Lower panel shows the schematic energy level diagram and charge transfer processes for photocatalysis and photovoltaic applications. Reprinted with permission from Ref. [20] Copyright 2015, Elsevier B.V.

HP filter. We have attributed the de-excitation of ZnO NPs via FRET to be responsible for the less photocatalytic activity of the LHAs in UV light excitation (no filter) as shown in the upper panel of Figure 5. On the other hand, visible light excitation (with filter) of the PbS QDs in the LHAs shuttles the photogenerated electron in the QDs through the CB of the ZnO NPs as shown in the lower panel of Figure 5. Overall for white light excitation of the LHAs, the photogenerated electron is sparsely available for the reduction of MB in the solution due to the above-mentioned two ultrafast mechanisms.

In order to investigate the efficacy of PbS-ZnO LHAs in photovoltaic application, we have performed photoelectrochemical measurements in a half cell geometry using the LHAs on ITO plate as anode and Pt as counter electrode [79]. For I–V measurement, the Ag/Ag+ couple are used as reference electrodes. The photocurrent measurement of ZnO and PbS-ZnO LHAs was carried out in order to better understand the electron transfer processes in terms of short-circuit current. The light source (100 mW cm^{-2}) was turned on and off every 60 s, and the obtained photocurrent values were continuously recorded. As shown in Figure 4B, under full light illumination, PbS-ZnO has greater photocurrent response than ZnO NPs on the ITO plate. The observation is consistent with the fact that the LHAs would able to harvest a wide band of light spectrum from UV to NIR in contrast to the ZnO NPs, which is expected to harvest only the UV region of the incident white light. The initial spike is observed due to the slower

recovery of the photoexcited holes from the electrolytes and is consistent with other studies reported in the literature [79]. Significant enhancement of the photocurrent in the presence of PbS in the proximity of ZnO NPs in contrast to the retardation of photocatalysis activity of the LHAs is rationalized in the following way. The photogenerated electron in the PbS as well as ZnO NPs is expected to be channelized to the ITO plate because of the lower potential as shown in the lower panel of Figure 5. The I–V characteristics of the LHAs in the presence of white light as shown in Figure 4C reveals a significantly higher short-circuit current compared to those of the ZnO NPs. The observation clearly indicates the importance of the presence of an ITO plate in the interfacial carrier dynamics of PbS-ZnO LHAs in photovoltaic application. Luther et al. have shown that the device composed of ZnO nanocrystals and 1.3 eV PbS QDs with gold as the top contact exhibits 3% efficiency and retained 95% of the starting efficiency after a 1000-h light soak in air without encapsulation [80]. In another publication, the J–V characteristics are investigated in a heterojunction PbS QD solar cell with the same cell architecture as above where ZnO/PbS interface and PbS/metal contact are described as two opposing diodes [81]. It was found that the Schottky barrier height is a function of the QD band gap energy and back contact metal work function. Thus, it is necessary to understand the interfacial carrier dynamics to maximize the cell efficiency. Jean et al. have demonstrated that the use of hydrothermally grown ZnO nanowires in ordered bulk heterojunction PbS QD photovoltaic devices achieved 4.3% power conversion efficiency [82].

3 Essential light-harvesting dynamics at semiconductor-metal interface

3.1 Photoselective dynamical events in ZnO-Au nanocomposites

In this section, we aimed to unravel the mechanism of pronounced intrinsic emission from colloidal ZnO and ZnO-Au NCs upon above band edge and below bandgap excitation [16]. To probe the correlation between the dynamics of photo-generated carrier trapping at the defect sites and kinetics of charge migration from ZnO and ZnO-Au semiconductors, MB degradation was examined under a different light irradiation. Time-resolved photoluminescence studies from a ZnO-Au NC colloidal dispersion reveal FRET dynamics from donor semiconductor to gold acceptor.

In the presence of Au NPs, the ZnO NP emission is quenched upon excitation at λ_{ex}=375 nm (below the bandgap) revealing the FRET from the donor ZnO NP to the Au acceptor. The spectral overlap of the ZnO emission spectrum with that of the Au absorption spectrum is shown in Figure 6A. The faster excited state lifetime of the ZnO-Au NC with respect to that of the free ZnO NP is clearly

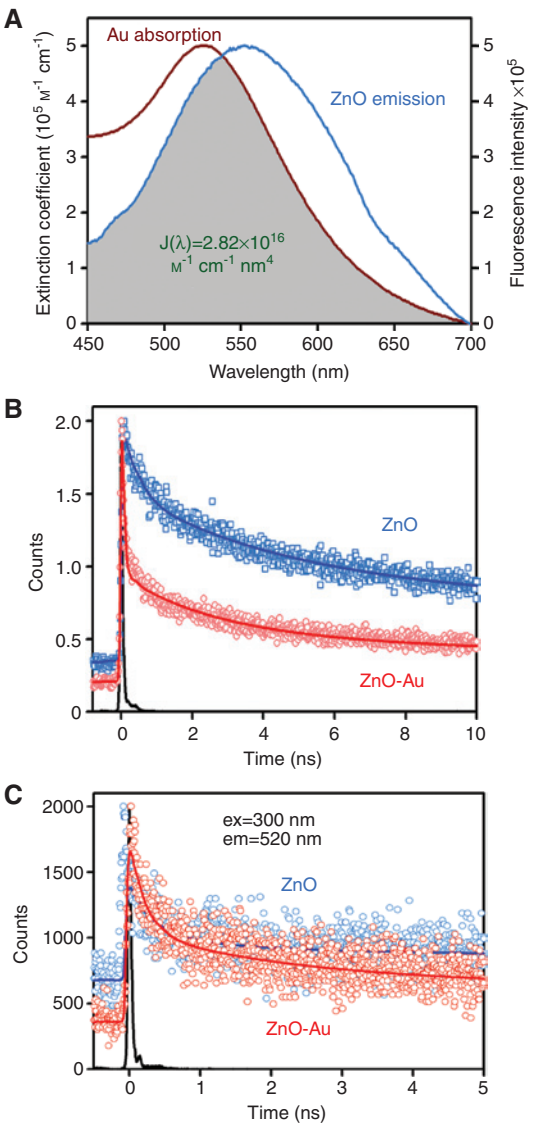

Figure 6: (A) SP band of Au NPs and emission spectra of ZnO NPs are shown. An overlapping zone between emission of ZnO NPs and absorption of acceptor Au is indicated as a gray-shaded zone. (B) The picosecond-resolved fluorescence transients of ZnO NPs, in the absence (blue) and presence of acceptor Au (red) (excitation at 375 nm) collected at 550 nm. (C) Picosecond-resolved luminescence transients of ZnO NPs in the presence and absence of Au NPs. The emissions from ZnO NPs and ZnO-Au NCs (probing at 520 nm) were detected with a 300-nm laser excitation.

noticeable from Figure 6B. Details of the spectroscopic parameters and the fitting parameters of the fluorescence decays are tabulated in Table 2. From the average lifetime calculation for the ZnO-Au NC, we obtain the effective distance between the donor and the acceptor, r_{DA}≈2.55 nm. Moreover, comparing the PL spectra of the bare ZnO NPs and ZnO-Au NCs upon excitation above the band edge, it was observed that the emission due to excitonic recombination is suppressed, while the defect-related emission is red shifted in the presence of Au NPs. In this respect, it is shown that the energy is transferred from the V_o^+ center to the Au NPs, which leads to a reduction in the PL intensity at 520 nm. The energy transfer efficiency (E) is found to be ~19% (Figure 6C), which is a much lower value compared to that of the below bandgap excitation (E=~85%). In retrospect, excited electrons are preferentially trapped by the V_O^{++} center, which is originated by V_O^+ by capturing a hole. The formation of V_O^{++} centers is more favorable upon band-edge excitation as the photogenerated holes have enough time to migrate during thermalization of highly excited electrons. This leads to more facile recombination of excited electrons via V_O^{++} centers, and this recombination pathway is supported by the appreciable red shift observed in ZnO-Au NCs upon above band-edge excitation. However, the decrease in band-edge emission intensity in the presence of Au NPs is well understood, whereby Au acts as a sink, which can store and shuttle photogenerated electrons [83, 84]. As per our understanding, the optical activity of the surface defect states in the overall emission of the semiconductor solely depends on the excitation wavelength.

3.2 Photoselective degradation of methylene blue in the presence of ZnO-Au nanocomposites

In order to investigate the role of Au NPs in promoting photogenerated charges in ZnO-Au NCs, the photo-reduction of a test contaminant MB was performed. In general, the higher the charge migration from the surface of the ZnO semiconductor, the faster will be the degradation of the surface-attached MB. In order to obtain different excitations, we have used three different types of filters placed on a homemade UV bath. The characteristics of the optical filters are shown in Figure 7A. In Figure 7B, the relative concentration (C_t/C_0) of MB in solution is plotted with respect to selective irradiation of light. To compare the photodegradation of MB in the presence of ZnO NPs and ZnO-Au NCs with a 420-HP filter, it is clearly shown that no considerable change in absorbance peak at 655 nm takes place upon Au SP excitation. It reveals that electron transfer from Au NPs to MB is not allowed upon direct excitation of Au. Upon, replacing the 420-HP filter with a 460-LP filter, we observed an increase in the photodegradation rates in the presence of Au NPs. This is attributed to improved charge separation in the presence of Au NPs, which also can store and shuttle excited electrons, thereby, suppressing recombination. Such Au NP-stabilized ZnO NPs behave as more efficient electron accumulators (at the CB) than the bare oxide. In retrospect, the photodegradation rate of MB was observed to decrease in the presence of Au NPs when we used combined optical filters of 320 HP and 460 LP. This happens because excited electrons of ZnO can easily occupy the defect centers and resonantly transfer their energy to Au NPs via nonradiative processes (FRET, as previously discussed). As a consequence, in the presence of Au, excited electrons are unable to migrate from the ZnO surface to perform the reduction of MB. Thus, it is important to note that the differences in rate constants are not significant, whereas considerable differences in the magnitude of total photodegradation are observed during above band edge and below bandgap excitation of ZnO and ZnO-Au NCs. This is due to the fact that the total number of active electrons available for carrying out MB degradation is different for ZnO and ZnO-Au NCs for any particular excitation. Our study clearly demonstrates that the role of incorporated metal on semiconductor for facilitating redox reactions is solely dependent on the excitation of the semiconductor, as schematically shown in Figure 8. Roy et al. [85] have used graphene-ZnO-Au NCs as photocatalysts for the reduction of nitrobenzene to aniline, with

Table 2: Dynamics of picosecond-resolved luminescence transients of ZnO NPs in the presence and absence of Au NPs.

Samples	Excitation wavelength (nm)	Detection wavelength (nm)	τ_1 (ns)	τ_2 (ns)	τ_3 (ns)	τ_{avg} (ns)
ZnO NP (bare)	375	550	47.58±0.45 (41%)	3.78±0.05 (23%)	0.280±0.03 (36%)	20.48±0.20
ZnO-Au NC	375	550	33.34±0.38 (8%)	2.60±0.06 (10%)	0.051±0.04 (82%)	2.97±0.04
ZnO NP (bare)	300	520	28.49±0.25 (22%)	0.83±0.07 (32%)	0.24±0.03 (46%)	6.64±0.09
ZnO-Au NC	300	520	24.35±0.31 (21%)	0.90±0.05 (19%)	0.16±0.03 (60%)	5.38±0.09

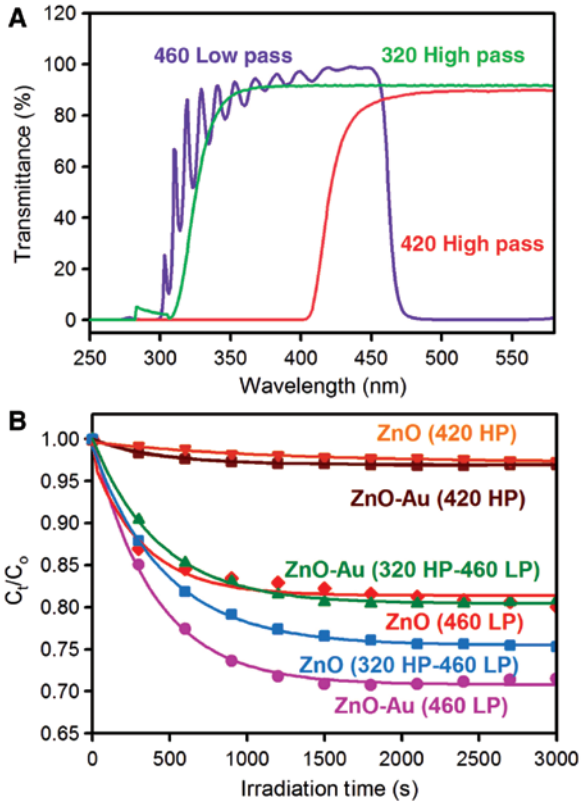

Figure 7: (A) The transmittance spectra of 320 high pass (green), 420 high pass (red) and 460 low pass (violet) optical filters are shown. (B) Plot of relative concentration (C_t/C_0) *versus* time for the degradation of MB (monitored at 655 nm) is shown. The degradation is performed in the presence of colloidal solutions of ZnO NPs and ZnO-Au NCs under different excitation conditions (parentheses indicate the optical filters used for the desired excitation). *Phys. Chem. Chem. Phys.* 2011, 13, 12488. Reproduced by permission of the PCCP Owner Societies.

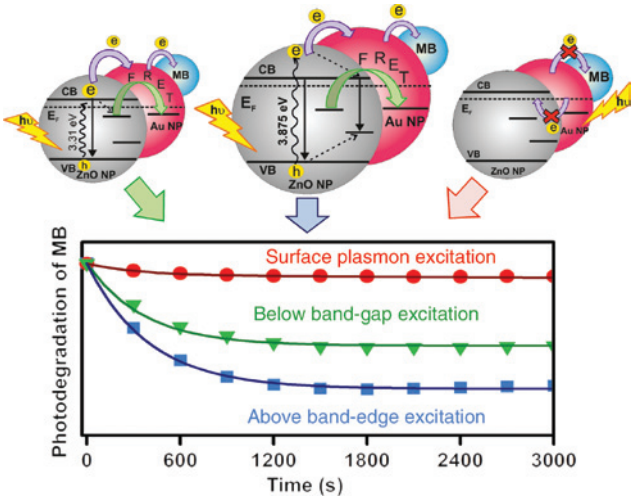

Figure 8: Schematic representation of the metal-semiconductor system: The system consists of a semiconductor ZnO NP (gray big ball) containing appreciable amounts of defect states on which a Au NP (red big ball) is fabricated. Methylene blue (small blue ball) is bound to the ZnO-Au NC by surface adsorption. The dynamics of charge separation and interparticle charge/energy migration of the entire structure is shown. Thereafter, photodegradation of methylene blue under different excitation conditions is also shown by a graph, which reveals the mediating role of Au NP in photocatalysis. *Phys. Chem. Chem. Phys.* 2011, 13, 12488. Reproduced by permission of the PCCP Owner Societies.

conversion efficiency of 97.8% within 140 min. The role of graphene and Au nanorods (NRs) in the photocatalytic activity of NCs was studied and found that graphene acted as an inhibitor toward the h^+/e^- recombination along with its excellent electron transport properties, whereas the Au NRs played a key role in efficient charge separation. In another report, the ZnO-Au NCs exhibits enhanced photocatalytic activity in MB degradation under a light source that has more than 95% (i.e. energy) of emitted photons between 400 and 800 nm [86]. Different nanostructures of ZnO-Au NCs such as hexagonal pyramid [87], nanoflowers [88], nanowires [89], and nanomultipods [90] are shown to exhibit efficient photocatalytic activity. Fragua et al. [91] have shown that the ZnO-Au NC film prepared by a single-step synthesis process demonstrates 4.5-fold enhanced photocatalytic properties for the decomposition of methyl orange upon sunlight exposure in comparison with ZnO films.

4 Ultrafast charge separation dynamics at semiconductor-organic dye interface

4.1 Electron transfer processes in porphyrin and metalloporphyrin functionalized semiconductor NPs

In this section, we aimed to understand the key photoinduced dynamics in organic dye (e.g. porphyrin)-sensitized devices for enhanced solar energy conversion. Here, we demonstrate our work on protoporphyrin-sensitized ZnO nanoparticles (PP-ZnO) for light-harvesting applications [27]. We have also explored the role of different metal ions in ultrafast photoinduced dynamics and their implications in photocatalysis. The femtosecond-resolved transient absorption spectra (excitation wavelength=350 nm) of the PP-ZnO nanohybrid in the presence and absence of iron and copper ions are shown in the wavelength range of 360–440 nm in Figure 9. It should be noted that the peaks at 370 nm and ~415 nm correspond to host ZnO band gap (3.37 eV) and soret band of the guest PP, respectively. The decay profiles at 370 nm detection wavelength revealing

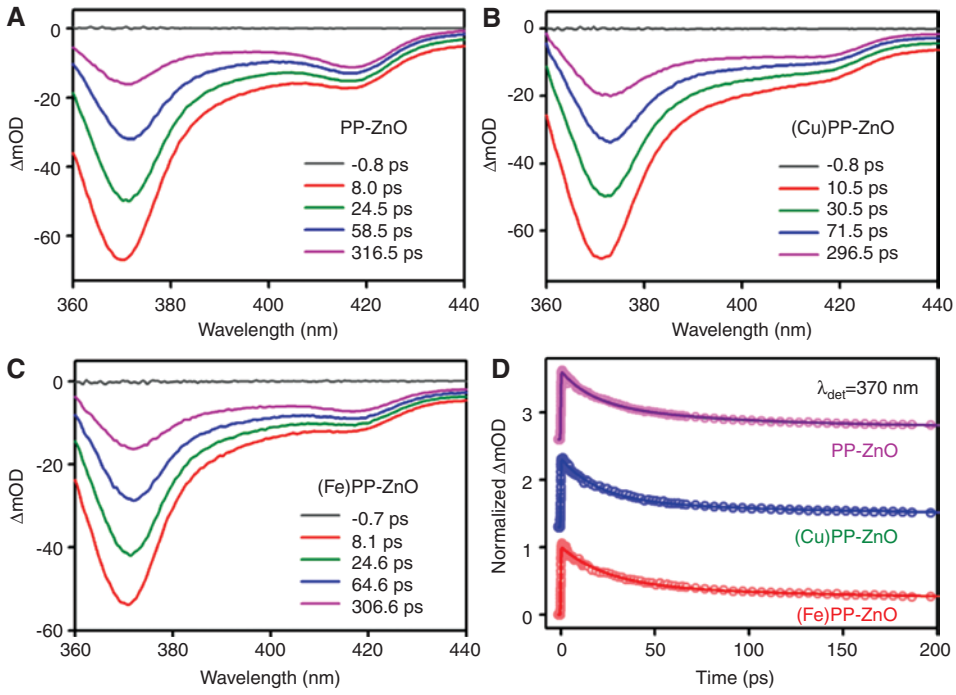

Figure 9: Transient absorption spectra of (A) PP-ZnO, (B) (Cu)PP-ZnO, and (C) (Fe)PP-ZnO at different time delays after excitation at 350 nm. (D) Time-resolved absorption changes of PP-ZnO (pink), (Cu)PP-ZnO (blue), (Fe)PP-ZnO (red) at probe wavelength 370 nm. All the spectra are studied in DMSO-water mixture (V/V). *Chem. Eur. J.* 2014, 20, 10475. Copyright 2014 WILEY-VCH Verlag GmbH & Co. KGaA, Weinheim.

ground state recovery of the excited ZnO in the nanohybrid in the presence and absence of the metal ions are shown in Figure 9D. The interference of PP absorption at the detection wavelength (370 nm) was ruled out in a set of control experiments with pure PP, revealing a different time scale (~ns) of ground-state bleach recovery. The numerical fitting of the transient absorption data of PP-ZnO shows decay time constants of 16.91 ps (48.63%), 88.64 ps (34.14%), and 7.44 ns (17.27%) for the ground state recovery of the host ZnO in the nanohybrid. While the nanohybrid in the presence of copper ion shows similar recovery time constants (16.20 ps (51.10%), 90.00 ps (30.98%) and 7.85 ns (17.92%)), a significant retardation of the time constants in the presence of the iron ions are observed (25.00 ps (58.29%), 204.23 ps (22.99%) and 11.01 ns (18.72%)). The time constants imply that the presence of iron ions can separate the electron-hole pairs of the excited ZnO NPs efficiently, leading to the slow recovery of the ground state of ZnO NPs in the nanohybrid. The transient absorption spectra of the Q bands of PP in the nanohybrids in the wavelength range 465–660 nm are shown in Figure 10A, C, E. From this figure, it is evident that the four numbers of Q bands present in the free base PP became essentially two in the presence of the iron and copper ions due to the higher molecular symmetry (D_{4h}) [92]. The decay profiles at soret and Q bands revealing the ground state recovery of the excited PP in the nanohybrid in the presence and absence of metal ions are shown in Figure 10B, D, F. The decay time constants are shown in Table 3. From Table 3 and Figure 10, it is clear that the presence of iron (III) ion delays the recovery of the excited PP, whereas the presence of copper ion exhibits similar time constants compared to PP in the nanohybrid. From the above observation on the ground state recovery dynamics, it is expected that upon UV excitation of ZnO in the nanohybrid in the presence of iron ion, the charge transfer is facilitated (longer exciton lifetime) and expected to reveal better photocatalysis [93].

The fluorescence decays of PP and PP-ZnO nanohybrid in the absence and presence of iron and copper ions are shown in Figure 11A and B (shorter time window) upon excitation of 409 nm and monitored at 630 nm. The fluorescence transients of PP and (Cu)PP are fitted with single exponential decays with a lifetime of 16.03 ns and 17.29 ns, respectively (Table 4). The increase in the excited state lifetime of PP in the presence of copper ion may be indicative of the stability of the PP molecule as reported earlier [45]. The time-resolved data of (Cu)PP rules out the possibility of charge transfer transitions from PP to Cu ion, and thus, the steady-state quenching of the PP emission in the presence of Cu can be attributed to the fast intersystem crossing, which is beyond our experimental time window [94]. However, the fluorescence decay profile of PP in the

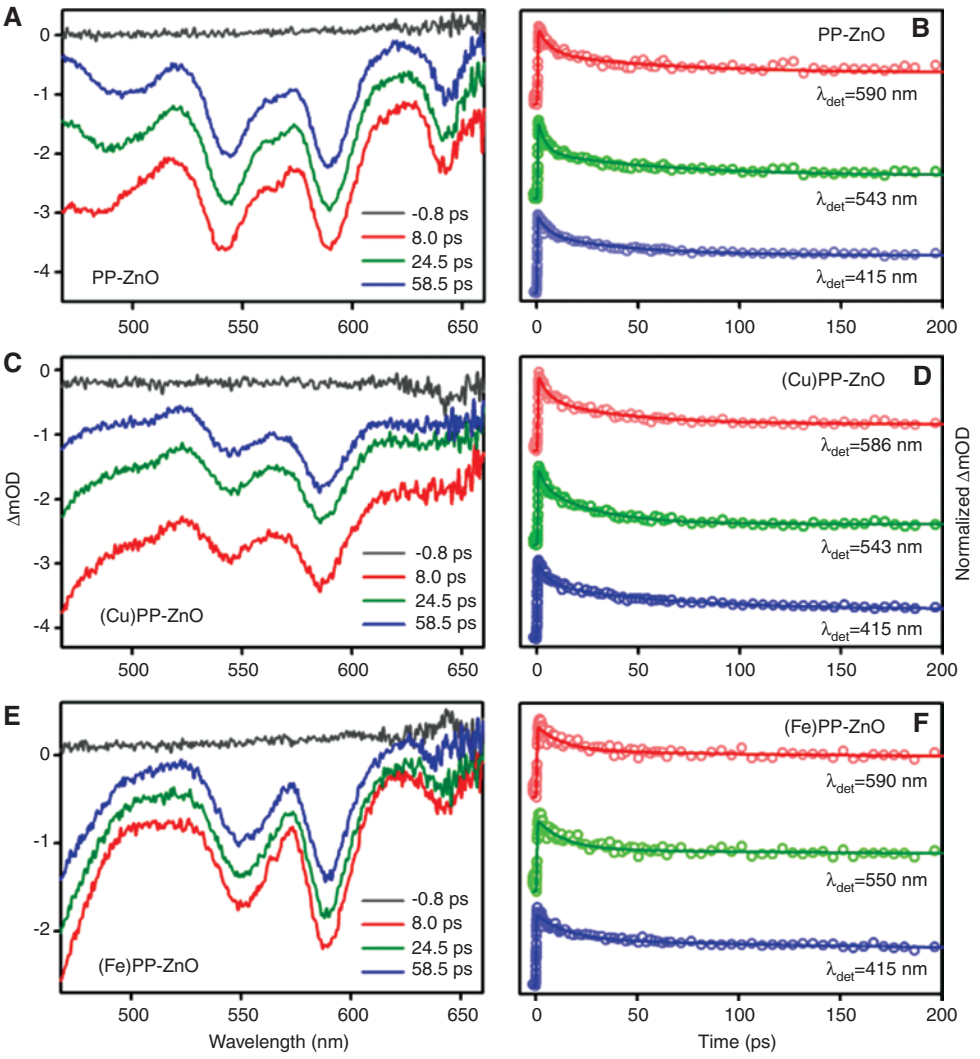

Figure 10: Transient absorption spectra of (A) PP-ZnO, (C) (Cu)PP-ZnO, and (E) (Fe)PP-ZnO at different time delays after excitation at 350 nm. Time-resolved absorption changes of (B) PP-ZnO, (D) (Cu)PP-ZnO, and (F) (Fe)PP-ZnO at different probe wavelengths. All the spectra are studied in DMSO-water mixture (V/V). *Chem. Eur. J.* 2014, 20, 10475. Copyright 2014 WILEY-VCH Verlag GmbH & Co. KGaA, Weinheim.

Table 3: Results of the fits of the transient absorption data at different probe wavelengths.

Sample	Monitored wavelength (nm)	τ_1 (ps)	τ_2 (ps)	τ_3 (ns)
PP-ZnO	370	16.91±0.22 (48.63%)	88.64±0.35 (34.14%)	7.44±0.21 (17.27%)
	415	6.00±0.20 (24.44%)	45.81±0.21 (26.54%)	1.60±0.12 (49.02%)
	543	3.73±0.20 (40.05%)	60.00±0.25 (29.92%)	1.60±0.11 (30.03%)
	590	5.84±0.20 (31.68%)	60.00±0.21 (26.11%)	1.60±0.15 (42.21%)
PP-Cu-ZnO	370	16.20±0.23 (51.10%)	90.00±0.30 (30.98%)	7.85±0.16 (17.92%)
	415	5.69±0.20 (27.87%)	61.45±0.25 (33.27%)	1.60±0.09 (38.86%)
	543	3.59±0.20 (23.68%)	27.52±0.20 (49.70%)	1.60±0.10 (26.62%)
	586	5.10±0.20 (31.20%)	40.93±0.22 (33.64%)	1.60±0.08 (35.16%)
PP-Fe-ZnO	370	25.00±0.25 (58.29%)	204.23±0.40 (22.99%)	11.01±0.25 (18.72%)
	415	15.00±0.21 (34.16%)	201.73±0.32 (17.90%)	1.60±0.08 (47.94%)
	550	13.41±0.21 (41.38%)	200.00±0.28 (7.56%)	1.60±0.09 (51.06%)
	590	13.06±0.20 (34.31%)	220.00±0.29 (11.82%)	1.60±0.10 (53.87%)

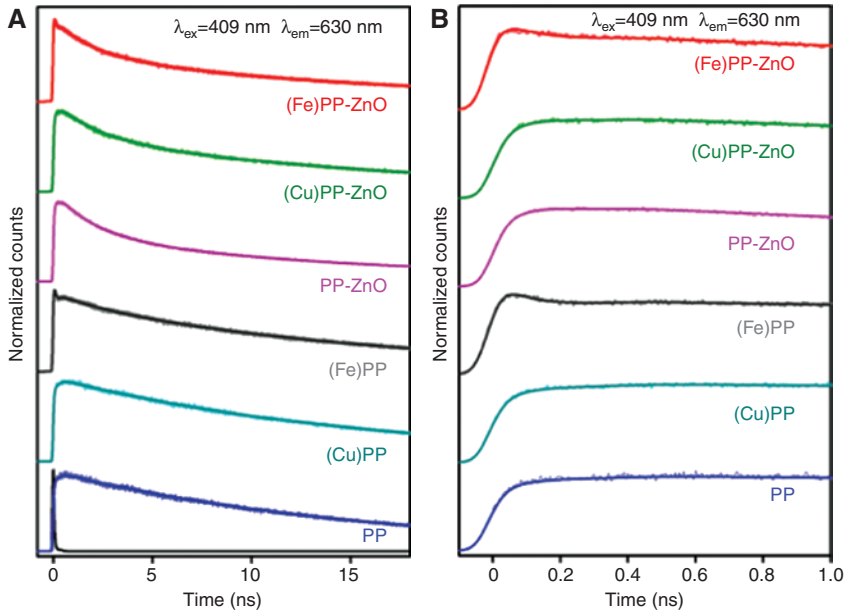

Figure 11: Fluorescence decay profile of PP (blue), Cu-PP (cyan), Fe-PP (dark gray), PP-ZnO (pink), (Cu)PP-ZnO (green), (Fe)PP-ZnO (red) in (A) longer time window and (B) shorter time window. All the spectra are studied in DMSO-water mixture (V/V). *Chem. Eur. J.* 2014, 20, 10475. Copyright 2014 WILEY-VCH Verlag GmbH & Co. KGaA, Weinheim.

Table 4: Picosecond-resolved fluorescence transients of PP, (Fe)PP, (Cu)PP, PP-ZnO, (Fe)PP-ZnO, and (Cu)PP-ZnO composites.[a]

Sample	τ_1 (ns)	τ_2 (ns)	τ_3 (ns)	τ_{avg}(ns)	$k_{nr}\times10^7(S^{-1})$
PP	16.03±0.03 (100%)			16.03±0.03	
(Fe)PP	16.61±0.05 (44.05%)	2.34±0.10 (5.95%)	0.048±0.03 (50%)	7.48±0.03	7.12±0.05
(Cu)PP	17.29±0.03 (100%)			17.29±0.03	
PP-ZnO	16.77±0.06 (43.75%)	2.06±0.03 (56.25%)		8.50±0.04	5.52±0.04
(Fe)PP-ZnO	16.64±0.06 (19.04%)	2.02±0.03 (26.67%)	0.024±0.03 (54.29%)	3.72±0.03	20.63±0.13
(Cu)PP-ZnO	16.98±0.05 (63.04%)	2.06±0.03 (36.96%)		11.47±0.04	2.48±0.03

[a]The emission (monitored at 630 nm) was detected with 409 nm laser excitation. k_{nr} represents nonradiative rate constant. Numbers in the parentheses indicate relative weightages.

presence of iron (III) shows shorter time constants of 0.048 ns (50%) and 2.34 ns (5.95%) along with 16.61 ns (44.05%) with an average excited state lifetime of 7.48 ns. The faster excited state lifetime of the PP in the presence of iron ion could be correlated to the electron transfer process from PP to iron ion.

As shown in Figure 11, in the PP-ZnO nanohybrid, the fluorescence decay profile is composed of a faster component of 2.06 ns (56.25%) and a longer component of 16.77 ns (43.75%), indicating an electron transfer process from the PP molecule to the ZnO NPs. While the slower component is consistent with the excited state lifetime of PP without ZnO, the faster one may be rationalized as the electron migration time from PP to the host ZnO. In the presence of copper ion in the excited state dynamics of the nanohybrid essentially remains unaltered. However, in the presence of iron (III), the decay profile of PP-ZnO shows an additional time component of 0.024 ns (54.29%), which is absent in either PP-ZnO and PP-ZnO in the presence of copper ion and can be rationalized as an electron migration pathway from PP to the centrally located Fe(III).

4.2 Photocatalytic activity of porphyrin and metalloporphyrin functionalized semiconductor NPs

In order to understand the modulation of photocatalysis of PP-ZnO in the presence of different metal ions, we have performed photocatalysis measurement of the nanohybrid in quartz cuvette under visible light as displayed in Figure 12A. The inclusion of iron ion in the PP-ZnO nanohybrid significantly reduced the photocatalytic

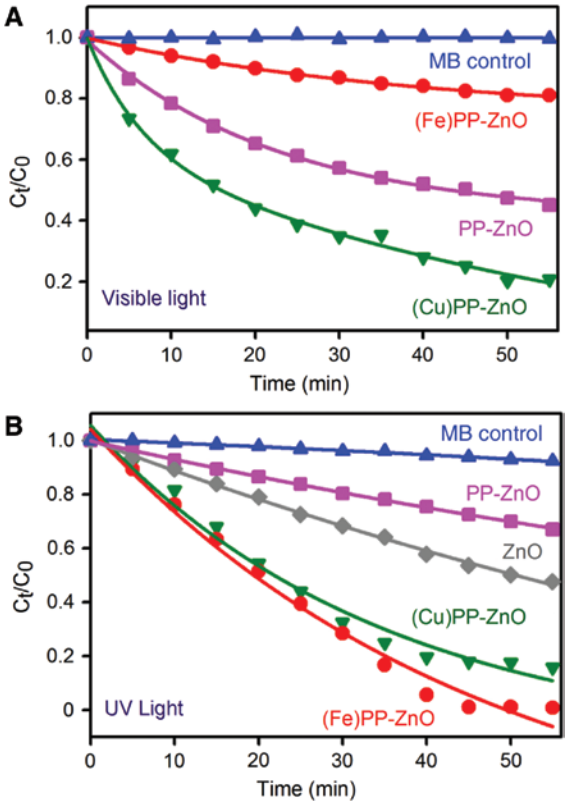

Figure 12: Photocatalytic degradation of MB in the presence of ZnO (dark gray), PP-ZnO (pink), (Fe)PP-ZnO (red), (Cu)PP-ZnO (green), and only MB (blue) nanohybrids under the (A) visible light and (B) UV light irradiation. *Chem. Eur. J.* 2014, 20, 10475. Copyright 2014 WILEY-VCH Verlag GmbH & Co. KGaA, Weinheim.

efficiency for the degradation of MB under visible light irradiation compared to that in the case of nanohybrid without metal and with copper ion. Relatively efficient photocatalysis of the nanohybrid with copper ion may be correlated with the additional structural stability of the PP in the nanohybrid. After 1-h visible light irradiation, 55% of MB was degraded in the presence of PP-ZnO. However, the presence of copper ion enhances the photocatalytic activity, and 80% MB degradation was observed. The copper ion provides stability to the PP moiety attached to the ZnO NPs, which leads to the enhancement in the photocatalytic activity. The photocatalytic activity of the PP-ZnO nanohybrid was suppressed significantly in the presence of iron ions, and only 17% MB degradation was observed. In this case, the photoexcited electrons of PP were trapped in the Fe(III) ions preferably instead of ZnO, which is evident from the transient absorption (Figure 10) and TCSPC studies (Figure 11). Our transient absorption studies on the nanohybrid at 350 nm excitation reveals longer excitonic lifetime in the presence of iron ion compared to that of either without metal or with copper ion. As mentioned earlier, incorporation of iron in the central cavity of the porphyrin under UV light irradiation is expected to offer better photocatalysis in contrast to that of the case under visible light irradiation. Another important fact is that any solar device should be exposed with some amount of UV radiation present in solar light (4–5%). Thus, in order to investigate the role of UV excitation, we have performed the photocatalytic activity of the nanohybrid in the presence and absence of metal ions under UV light irradiation as shown in Figure 12B. Under UV light irradiation, 55% MB degradation was observed in the presence of ZnO NPs, whereas in the presence of PP-ZnO nanohybrid, only 25% MB degradation was evidenced. Under UV irradiation, the ZnO valence band (VB) electrons are excited to the CB, which can reduce dioxygen to superoxide, eventually leading to the production of hydroxyl radicals ($OH^{\cdot}$). The hole in the valence band accept an electron from water to generate a hydroxyl radical ($OH^{\cdot}$), which can also participate in the degradation process. Thus, the efficiency of the nanohybrid essentially depends on the number of photo-generated carrier (electrons and holes) and their exciton lifetime. In the case of (Fe)PP-ZnO, the photo-generated electron is shown to be trapped in the centrally located iron moiety of the nanohybrid, and ROS generation is essentially governed by the hole in the valence band and enhanced exciton lifetime (as evidenced from transient absorption, discussed above). On the other hand, for (Cu)PP-ZnO, ROS generation is expected to be governed by the photo-generated carriers (both electrons and holes); however, it may not acquire extra advantage from the exciton lifetime (as evidenced from transient absorption), revealing comparable photocatalysis with respect to that in the (Fe)PP-ZnO nanohybrid. The significant retardation of photocatalysis in the case of PP-ZnO without metalation may be rationalized from the photo-reduction of the attached PP by the photo-excited electron from ZnO. We have observed significant photo-bleaching of PP in PP-ZnO nanohybrid in the absence of metal ions under UV irradiation. The overall mechanistic pathway of the photo-catalysis of the nanohybrid upon visible and UV irradiation is shown in Figure 13. Recently, Dabrowski et al. have performed photophysical and photochemical studies on 5, 10, 15, 20-tetrakis(2,6-difluoro-5-N-methylsulfamylophenyl) porphyrin and its cobalt(III) and zinc(II) complexes and found that that impregnation of TiO_2 (P25) with functionalized porphyrins can improve its photoactivity [95]. The photocatalytic activity of the complexes were examined by photodegradation of a synthetic opioid

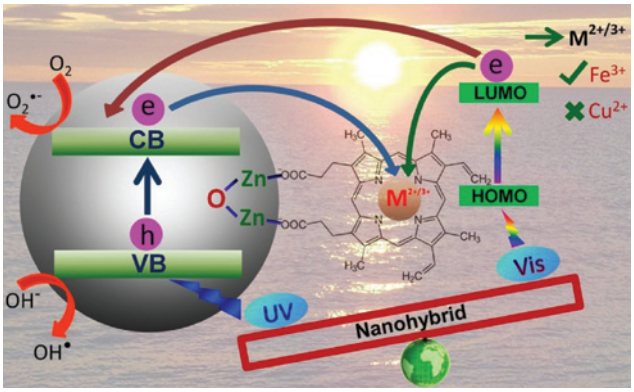

Figure 13: Schematic representation of ultrafast dynamical processes in protoporphyrin-zinc oxide nanohybrid in the presence of different central metal ions under UV and visible light excitation. *Chem. Eur. J.* 2014, 20, 10475. Copyright 2014 WILEY-VCH Verlag GmbH & Co. KGaA, Weinheim.

such as tramadol hydrochloride (TRML) and a model pollutant, 4-chlorophenol, in aqueous solution under visible light irradiation (λ>400 nm). The Zn (II) complex exhibited a superior photocatalytic performance toward TRML degradation. Radivojevic et al. have investigated a new mode of binding chromophores such as metalloporphyrins and metallophthalocyanines to oxide surfaces in DSSC through group IV metal ions (Hf (IV) and Zr (IV)), which protrudes sufficiently from the chromophores to concomitantly bind to oxide surfaces [96]. The unique way of attaching dyes to the surface facilitating electron injection to the semiconductor may be due to the coupling of the dye orbitals with the Hf(IV) and Zr(IV) orbitals and simultaneously to the 3d orbitals of the CB of TiO_2. In another study, the dye/semiconductor binding is described with a heterogeneous geometry where the Zn-porphyrin molecules are attached to the TiO_2 surface with a distribution of tilt angles [97]. It was shown that the binding angle determines the porphyrin-semiconductor electron transfer distance, and charge transfer occurs through space, rather than through the bridge connecting the porphyrin to the surface. In one of our recent publications, we have functionalized zinc phthalocyanine (ZnPc) with two carboxyl groups containing a biologically important ligand, tartrate, using a facile wet chemistry route and duly sensitized zinc oxide (ZnO) to form nanohybrids for application in photocatalytic devices [28]. The efficiency of the material for photocatalysis under red light irradiation was found to be significantly enhanced compared to bare ZnO. Thus, the semiconductor-dye nanohybrids have proven to be efficient functional materials for solar energy harvesting applications.

5 Key ultrafast light-harvesting dynamics at semiconductor-conducting polymer interface

5.1 Enhanced charge separation and FRET at heterojunctions between semiconductor nanoparticles and conducting polymer nanofibers

In order to investigate the interfacial charge separation at the nanoheterojunction between poly(1, 4-diphenylbutadiyne) nanofibers and ZnO nanoparticles (PDPB-ZnO), which is the key step for efficient light harvesting, the photoinduced carrier dynamics is monitored by steady state and picoseconds-resolved fluorescence studies. Room temperature PL spectra of PDPB exhibit a strong dependency on the excitation wavelength as shown in Figure 14A. The emission peak is red shifted from 410 nm to 650 nm at different excitation wavelengths from 350 nm to 600 nm. This suggests the presence of multiple emitting states in the polymer nanofibers, which are associated with the wide extend of conjugation in the different segments having various oligomeric and polymeric chains. This kind of phenomenon is well documented in the field of conjugated oligomers and polymers [98]. It has to be noted that the emission at 650 nm for the excitation wavelengths above 510 nm is originated from the conjugated polymer chain, which acts as molecular wire. The multiple photoluminescence are further investigated from the excitation spectra as shown in Figure 14B. The excitation spectra of PDPB at different detection wavelengths reveal a maximum at 340 nm, which is consistent with the absorption spectra of PDPB. As the detection wavelength shifts from 420 nm to 600 nm, the tail of the excitation spectra extends to the visible region due to the extended conjugation in PDPB nanofibers. Moreover, the excitation spectra monitored at a wavelength of 650 nm shows a peak around 590 nm, which can be attributed to the long conjugated polymeric chain. In contrast, the emission spectrum of the PDPB-ZnO LHNH is independent on the excitation wavelength from 350 nm to 470 nm due to oligomeric units of the polymer, as shown in Figure 14C. However, the emission spectrum of LHNH illustrates a peak at 665 nm upon excitation at 600 nm, attributed to polymer chains. This observation clearly indicates the strong electronic interaction between semiconducting PDPB nanofibers and ZnO NPs. Owing to the formation of nanoheterojunction with a large interfacial area, the mobility of the excitons toward the interface is facilitated [99]. Consequently, the excited

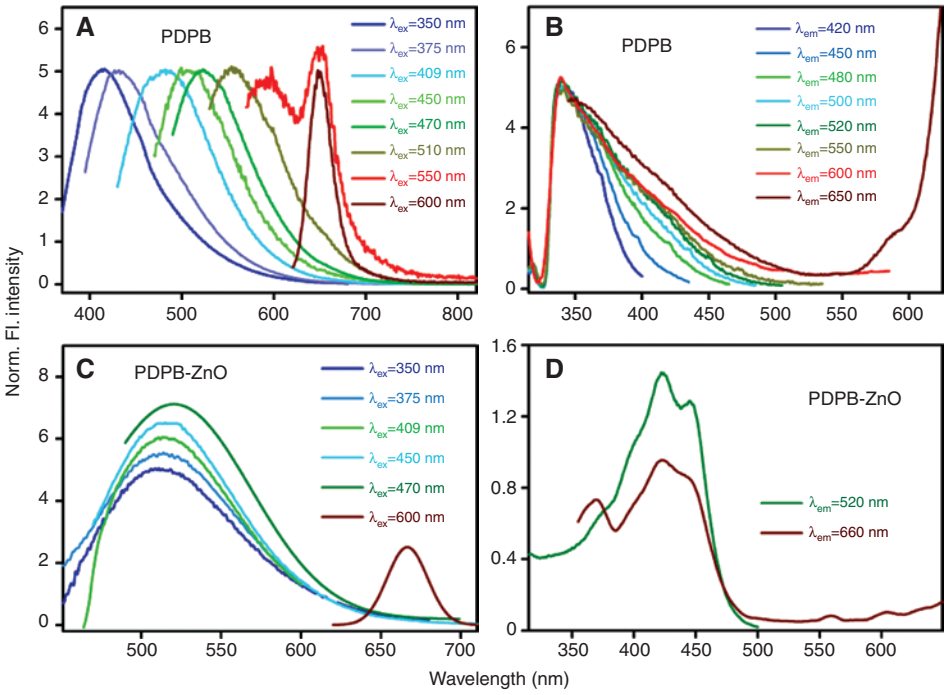

Figure 14: Room temperature PL spectra of (A) PDPB, (C) PDPB-ZnO at different excitation wavelengths. The excitation spectra of (B) PDPB, (D) PDPB-ZnO monitored at different emission maxima are shown. All spectra were recorded in ethanol. Reproduced from Ref. [22].

electrons from the polymer nanostructures instantly transfer to the ZnO NPs and eventually deexcite through defect centers located at the near surface that arise from oxygen vacancies [65]. The excitation spectrum of PDPB-ZnO as shown in Figure 14D at the detection wavelength 520 nm reveals two distinct peaks at 420 nm and 445 nm, which are consistent with the bandgap absorption of the oligomers.

The room temperature PL spectra of PDPB nanofibers show an emission peak at 485 nm upon the excitation at 409 nm, as shown in Figure 15A. The intensity of the emission peak decreases considerably and is red shifted to 520 nm when the polymers are attached to the ZnO NPs. The shift is due to the strong electronic interaction and energy level alignment at the nanoheterojunction. The inset of Figure 15A shows the corresponding excitation spectra. The picoseconds-resolved fluorescence decays (Figure 15C) of PDPB and PDPB-ZnO LHNH were measured upon excitation with 409 nm laser and monitored at a wavelength of 520 nm. In the case of PDPB-ZnO LHNH, the decay curve of PDPB shows significant shorter lifetime of 30 ps (74%) compared to that of PDPB; 140 ps (45%) (Table 5). The observed decrease in lifetime can be correlated to the electron transfer process from PDPB oligomers to the ZnO NPs. The charge separation from polymeric chain of PDPB to ZnO NPs is also monitored from steady state and time resolved spectroscopy, as shown in Figure 15B and D, respectively. The steady-state emission peak decreases and is red shifted to 665 nm for PDPB-ZnO LHNH upon excitation at 620 nm. The inset of Figure 15B shows the corresponding excitation spectra. As shown in Figure 15D, the fluorescence decay curve for PDPB upon excitation at 633 nm shows an intrinsic buildup with a rise component of 290 ps (monitored at 660 nm) due to delocalization of electrons in the conjugated polymeric chain. The emission decay curve of PDPB is fitted with a rise followed by single exponential decay function with a lifetime of 1.58 ns. However, the decay curve of PDPB-ZnO LHNH deviates from single exponential to biexponential showing one significant shorter lifetime of 30 ps (87%) and a longer lifetime of 1.24 ns (13%). Hence, the efficient photoinduced charge separation takes place at the nanoheterojunction where electrons are transferred from the conjugated polymer nanofibers to the ZnO NPs, and holes remain in the polymers.

After studying the interfacial dynamics at the nanoheterojunction using ZnO NPs with approximate size ~20 nm, which does not have intrinsic defect state emission, ZnO NPs (~5 nm) were synthesized *in situ* on PDPB nanofibers to investigate the role of defect states in the photoinduced charge transfer processes. The ZnO NP (~5 nm) has an intrinsic defect state emission as shown in Figure 16A. Inset of Figure 16A illustrated the absorption spectrum of the corresponding ZnO NPs. The emission

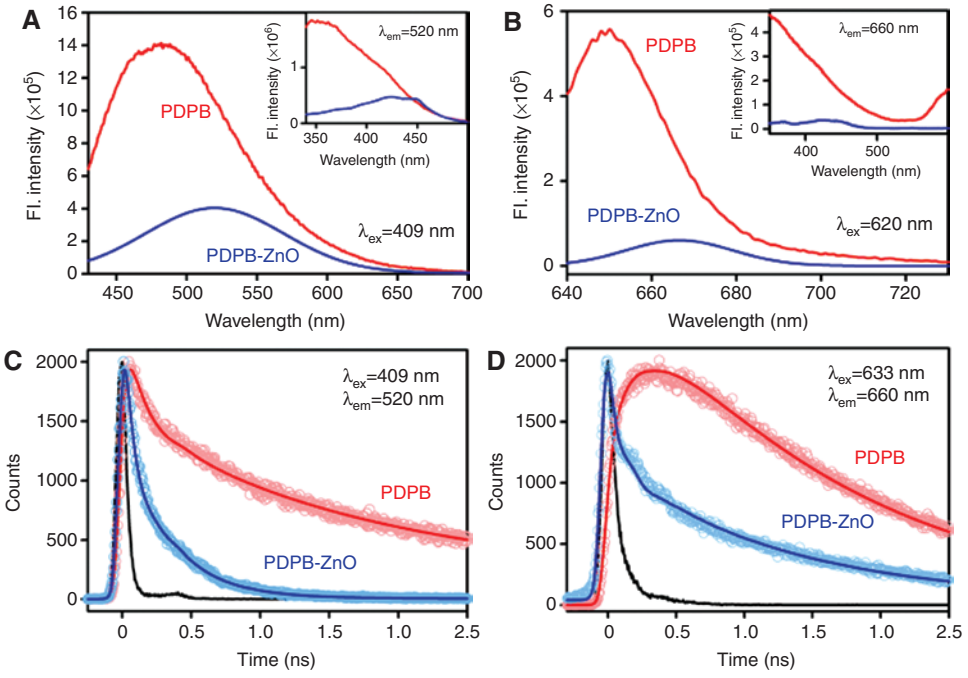

Figure 15: PL spectra of PDPB, PDPB-ZnO at excitation wavelengths (A) 409 nm and (B) 633 nm. The inset shows excitation spectra monitored at 520 nm and 660 nm, respectively. Fluorescence decay profiles of PDPB and PDPB-ZnO at (B) 520 nm (excitation at 409 nm) (D) 660 nm (excitation at 633 nm). Reproduced from Ref. [22].

Table 5: Dynamics of picosecond-resolved luminescence transients of PDPB and PDPB-ZnO LHNH.[a]

Sample	Excitation wavelength (nm)	Detection wavelength (nm)	τ_1 (ns)	τ_2 (ns)	τ_3 (ns)
PDPB	409	520	0.14±0.03 (45.4%)	1.40±0.05 (34.8%)	4.85±0.10 (19.8%)
PDPB-ZnO	409	520	0.03±0.03 (74.2%)	0.30±0.03 (23.8%)	2.21±0.08 (2.0%)
PDPB	633	650	0.29±0.05 (-21%)	1.58±0.08 (121%)	
PDPB-ZnO	633	650	0.03±0.03 (86.7%)	1.24±0.05 (13.3%)	

[a]Numbers in the parentheses indicate relative weightages.

intensity decreases when ZnO NPs are attached to the PDPB nanofibers (inset of Figure 16B showed the TEM image of PDPB-ZnO, 5 nm), which can be attributed to photoinduced non-radiative processes from ZnO NPs to the PDPB nanofibers. There is significant spectral overlap between ZnO NP emission and PDPB absorption as shown in Figure 16B, which leads to a probable energy transfer. The picoseconds-resolved fluorescence decay profile of the donor ZnO NPs in the presence and absence of the acceptor PDPB were obtained upon excitation with a 375-nm laser and monitored at 500 nm (P_1) and 550 nm (P_2) (Figure 16C and D, respectively). A shorter excited state lifetime of the ZnO NPs is clearly observed in the presence of PDPB. Details of the spectroscopic fitting parameters of the fluorescence transients are tabulated in Table 6. From FRET calculations, the distance between the donor ZnO NPs and acceptor PDPB nanofibers are determined to be 3.4 nm and 3.1 nm for the P_1 and P_2 states, respectively. The FRET distance is consistent with the size of the ZnO NPs (radius=2.5 nm). The energy transfer efficiency is calculated to be 64% and 70% from the P_1 and P_2 states, respectively. This observation confirms the proximity between the PDPB and ZnO as well as UV light harvesting in the LHNH via energy transfer from ZnO to PDPB nanofibers.

5.2 Photocatalytic activity of PDPB-ZnO heterojunctions

In order to investigate the manifestation of the interfacial charge transfer dynamics in PDPB-ZnO heterojunction, the photocatalytic activity has been studied using methyl

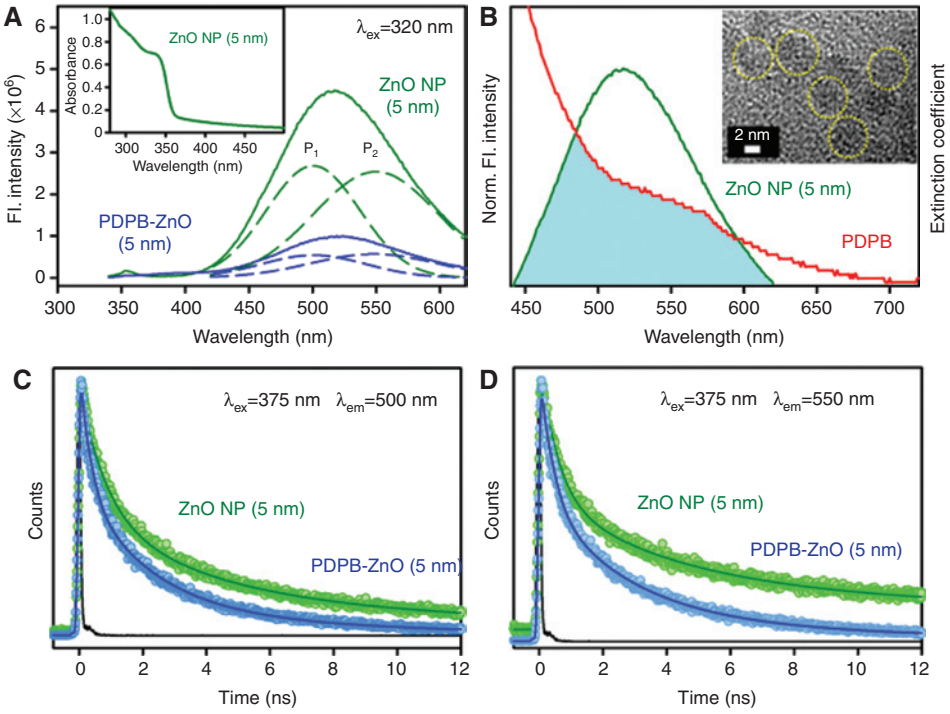

Figure 16: (A) Room temperature PL spectra of ZnO NPs (green) and PDPB-ZnO LHNH (blue) are shown. The excitation wavelength was at 320 nm. The broad emission band is composed of two components, P1 (500 nm) and P2 (555 nm). Inset shows the absorption spectrum of ZnO NPs (~5 nm). (B) Shows the overlap of the ZnO NP emission and PDPB absorption. Inset shows the HRTEM image of *in situ* synthesized ZnO NPs (~5 nm) on PDPB nanofibers. The picosecond-resolved fluorescence transients of ZnO NPs (excitation at 375 nm) in the absence (green) and in the presence of PDPB (blue) collected at (C) 500 nm and (D) 555 nm are shown. Reproduced from Ref. [22].

Table 6: Dynamics of picosecond-resolved luminescence transients of PDPB and PDPB-ZnO LHNH.[a]

Sample	Excitation wavelength (nm)	Detection wavelength (nm)	τ_1 (ns)	τ_2 (ns)	τ_3 (ns)	τ_{avg} (ns)
ZnO NP (5 nm)	375	500	0.82±0.05 (51.8%)	4.22±0.08 (40.7%)	29.30±0.11 (7.5%)	4.34±0.06
PDPB-ZnO	375	500	0.27±0.03 (53.3%)	2.15±0.05 (39.5%)	7.8±0.08 (7.2%)	1.55±0.05
ZnO NP (5 nm)	375	550	0.52±0.06 (51.3%)	4.01±0.08 (35.0%)	35.12±0.15 (13.7%)	6.48±0.08
PDPB-ZnO	375	550	0.34±0.03 (53.2%)	2.63±0.08 (39.8%)	9.89±0.10 (7%)	1.91±0.06

[a]Numbers in the parentheses indicate relative weightages.

orange (MO) as a model pollutant. The photocatalytic activity of the LHNH for degradation of MO under UV-VIS and Visible light was compared with ZnO NPs and PDPB nanofibers as a control experiment (Figure 17A and B). Figure 17A demonstrates the efficient photocatalytic activity of PDPB-ZnO LHNH (74%) in comparison to both counter parts (PDPB, 18% and ZnO, 40%) under 240-min UV-VIS light irradiation (λ≥365 nm). Figure 17B shows that the PDPB-ZnO LHNH is also very active for photocatalytic degradation of MO under 120-min visible light irradiation. However, ZnO NPs having a wide bandgap did not show any visible light activity. The activity of the polymer nanostructures is much lower, ~17% in comparison to PDPB-ZnO LHNH (80%) under similar illumination conditions. These observations suggest that due to efficient charge separation at the interface between PDPB and ZnO, the PDPB-ZnO LHNH is suitable for solar light harvesting. A large number of reactive species including h^+, $^{\cdot}OH$, and $O_2^{\cdot-}$ are involved in the photocatalytic oxidation process [100]. Hence, the effects of free radical scavengers on the degradation of MO were examined to elucidate the reaction mechanism. To investigate the role of the excess electrons, Cu^{2+} was used as a scavenger (it reacts with electron to yield Cu^+). Tertiary butyl alcohol (TBA) was introduced as the scavenger of $^{\cdot}OH$, and ethylenediaminetetraacetic acid (EDTA) was adopted to quench the holes (h^+) [101].

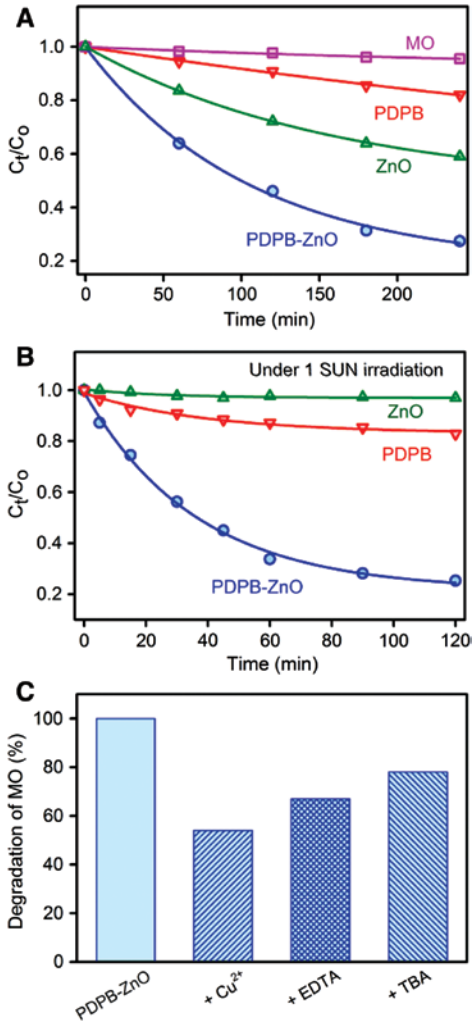

Figure 17: Photocatalytic activity of PDPB nanofibers, ZnO nanoparticles and PDPB-ZnO light-harvesting nanoheterojunction. Photocatalytic degradation of MO in the presence of PDPB (red), ZnO (green), and PDPB-ZnO (blue) under (A) UV light, (B) visible light (1 sun) irradiation. (C) Effect of Cu^{2+}, EDTA, and TBA on the photocatalytic activity of PDPB-ZnO LHNH. The photodegradation reaction of MO (initial concentration $C_0=0.3\times10^{-4}$ M) was carried out in a 10-mm optical path quartz cell reactor containing 3.5 ml of a model solution with a concentration of 1 $g.l^{-1}$ of the PDPB-ZnO, PDPB nanofiber (0.2 $g.l^{-1}$), and ZnO NPs (1 $g.l^{-1}$). Reproduced from Ref. [22].

As a consequence of quenching, the photocatalytic oxidation reaction is partly suppressed. The effects of a series of scavengers on the degradation efficiency of MO are shown in Figure 17C. The degradation efficiency of PDPB-ZnO photocatalyst for MO is reduced to 44% after adding Cu^{2+}. A similar trend is observed after the addition of EDTA and TBA. The corresponding photodegradation efficiencies decreased to 49% and 55%, respectively. According to the above experimental results, it can be clearly seen that $O_2^{\cdot-}$ and h^+ are the main reactive species in the photocatalytic oxidation process of MO, whereas $^{\cdot}OH$ has a minimal effect on this process. The overall dynamical processes and enhanced photocatalytic activity is schematically shown in Figure 18. The modification of ZnO NPs with PDPB nanofibers was the first report where polymer nanostructures have been used in order to form the nanoheterojunction. Previously, several studies have been reported on the modification of ZnO with bulk polymers [102, 103]. Abdiryim et al. have reported that poly(3,4-ethylenedioxythiophene)/zinc oxide (PEDOT/ZnO) NCs prepared by a simple solid state heating method exhibits enhanced photocatalytic activity under both UV light and natural sunlight irradiation [104].

6 Conclusion

In this review, four specific strategies for the modification of semiconductor nanostructures for visible light-responsive activity have been discussed. In all kinds of modifications, ultrafast excited state charge transfer across oxide surfaces is involved. Thus, a detail spectroscopic investigation is necessary to fully understand the microscopic mechanism as the band alignments and carrier dynamics across the interfaces are recognized as the key factors for light-harvesting applications. We have discussed the photoinduced processes in PbS-ZnO LHAs, ZnO-Au nanocomposites, protoporphyrin-sensitized ZnO nanoparticles, and PDPB-ZnO nanoheterojunction. The studies unravel the strong correlation between the ultrafast processes and their implications in detoxification of pollutants in water. The exploration of interfacial carrier dynamics at

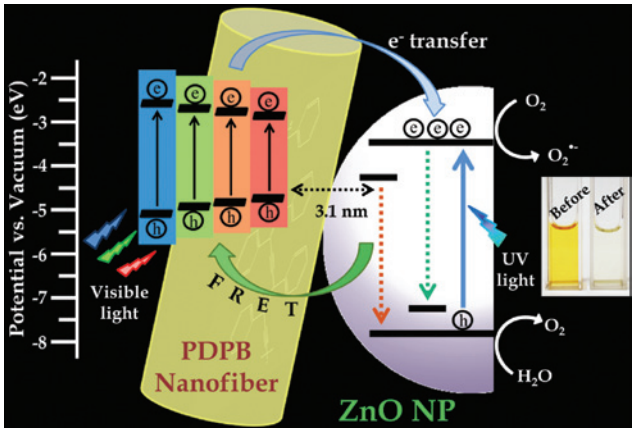

Figure 18: Schematic presentation of the co-sensitization of different PDPB oligomers to ZnO NPs and the interfacial carrier dynamics at the heterojunction showing the photocatalytic degradation of MO in aqueous solution.

the heterostructure interface will be helpful in improving the design and efficiency of future solar energy-harvesting devices.

Acknowledgments: We thank DST (India) for financial grants DST/TM/SERI/2k11/103 and SB/S1/PC-011/2013. We also thank DAE (India) for financial grant, 2013/37P/73/BRNS. We would like to thank our colleagues and collaborators whose contributions over the years, acknowledged in the references, have been priceless in the successful evolution of the work in this area. In particular, we thank Dr. Soumik Sarkar, Dr. Abhinandan Makhal, Mr. Prasenjit Kar, Dr. Tanujjal Bora, Dr. Sunandan Baruah, Dr. Omar F. Mohammed, Dr. Hynd Remita, Dr. Srabanti Ghosh, Prof. Peter Lemmens, and Prof. Joydeep Dutta.

References

[1] Chu S, Majumdar A. Opportunities and challenges for a sustainable energy future. *Nature* 2012, 488, 294–303.
[2] Turner JA. Sustainable hydrogen production. *Science* 2004, 305, 972–974.
[3] Chen X, Li C, Gratzel M, Kostecki R, Mao SS. Nanomaterials for renewable energy production and storage. *Chem. Soc. Rev.* 2012, 41, 7909–7937.
[4] Fujishima A, Honda K. Electrochemical photolysis of water at a semiconductor electrode. *Nature* 1972, 238, 37–38.
[5] O'Regan B, Gratzel M. A low-cost, high-efficiency solar cell based on dye-sensitized colloidal TiO_2 films. *Nature* 1991, 353, 737–740.
[6] Serpone N, Emeline AV. Semiconductor photocatalysis – past, present, and future outlook. *J. Phys. Chem. Lett.* 2012, 3, 673–677.
[7] Legrini O, Oliveros E, Braun AM. Photochemical processes for water treatment. *Chem. Rev.* 1993, 93, 671–698.
[8] Fox MA, Dulay MT. Heterogeneous photocatalysis. *Chem. Rev.* 1993, 93, 341–357.
[9] Hoffmann MR, Martin ST, Choi W, Bahnemann DW. Environmental applications of semiconductor photocatalysis. *Chem. Rev.* 1995, 95, 69–96.
[10] Schneider J, Matsuoka M, Takeuchi M, Zhang J, Horiuchi Y, Anpo M, Bahnemann DW. Understanding TiO_2 photocatalysis: Mechanisms and materials. *Chem. Rev.* 2014, 114, 9919–9986.
[11] Hernandez-Alonso MD, Fresno F, Suarez S, Coronado JM. Development of alternative photocatalysts to TiO_2: challenges and opportunities. *Energy Environ. Sci.* 2009, 2, 1231–1257.
[12] Chen C, Li X, Ma W, Zhao J, Hidaka H, Serpone N. Effect of transition metal ions on the TiO_2-assisted photodegradation of dyes under visible irradiation: a probe for the interfacial electron transfer process and reaction mechanism. *J. Phys. Chem. B* 2002, 106, 318–324.
[13] Asahi R, Morikawa T, Ohwaki T, Aoki K, Taga Y. Visible-light photocatalysis in nitrogen-doped titanium oxides. *Science* 2001, 293, 269–271.
[14] Lu N, Quan X, Li J, Chen S, Yu H, Chen G. Fabrication of boron-doped TiO_2 nanotube array electrode and investigation of its photoelectrochemical capability. *J. Phys. Chem. C* 2007, 111, 11836–11842.
[15] Li XZ, Li FB. Study of Au/Au3+-TiO2 photocatalysts toward visible photooxidation for water and waste water treatment. *Environ. Sci. Technol.* 2001, 35, 2381–2387.
[16] Sarkar S, Makhal A, Bora T, Baruah S, Dutta J, Pal SK. Photo-selective excited state dynamics in ZnO-Au nanocomposites and their implications in photocatalysis and dye-sensitized solar cells. *Phys. Chem. Chem. Phys.* 2011, 13, 12488–12496.
[17] Zhang Z, Wang W, Wang L, Sun S. Enhancement of visible-light photocatalysis by coupling with narrow-band-gap semiconductor: s case study on Bi2S3/Bi2WO6. *ACS Appl. Mater. Interfaces* 2012, 4, 593–597.
[18] Jiang J, Zhang X, Sun P, Zhang L. ZnO/BiOI heterostructures: photoinduced charge-transfer property and enhanced visible-light photocatalytic activity. *J. Phys. Chem. C* 2011, 115, 20555–20564.
[19] Li G-S, Zhang D-Q, Yu JC. A new visible-light photocatalyst: CdS quantum dots embedded mesoporous TiO_2. *Environ. Sci. Technol.* 2009, 43, 7079–7085.
[20] Sardar S, Kar P, Sarkar S, Lemmens P, Pal SK. Interfacial carrier dynamics in PbS-ZnO light harvesting assemblies and their potential implication in photovoltaic/photocatalysis application. *Sol. Energ. Mat. Sol. Cells* 2015, 134, 400–406.
[21] Zhang H, Zong R, Zhao J, Zhu Y. Dramatic visible photocatalytic degradation performances due to synergetic effect of TiO_2 with PANI. *Environ. Sci. Technol.* 2008, 42, 3803–3807.
[22] Sardar S, Kar P, Remita H, Liu B, Lemmens P, Pal SK, Ghosh S. Enhanced charge separation and FRET at heterojunctions between semiconductor nanoparticles and conducting polymer nanofibers for efficient solar light harvesting. *Sci. Rep.* 2015, 5, 17313.
[23] Sarkar S, Makhal A, Bora T, Lakhsman K, Singha A, Dutta J, Pal SK. Hematoporphyrin–ZnO nanohybrids: twin applications in efficient visible-light photocatalysis and dye-sensitized solar cells. *ACS Appl. Mater. Interfaces* 2012, 4, 7027–7035.
[24] Sardar S, Sarkar S, Myint MTZ, Al-Harthi S, Dutta J, Pal SK. Role of central metal ions in hematoporphyrin-functionalized titania in solar energy conversion dynamics. *Phys. Chem. Chem. Phys.* 2013, 15, 18562–18570.
[25] Sardar S, Chaudhuri S, Kar P, Sarkar S, Lemmens P, Pal SK. Direct observation of key photoinduced dynamics in a potential nano-delivery vehicle of cancer drugs. *Phys. Chem. Chem. Phys.* 2015, 17, 166–177.
[26] Sardar S, Kar P, Pal SK. The impact of central metal ions in porphyrin functionalized ZnO/TiO_2 for enhanced solar energy conversion. *J. Mat. NanoSci.* 2014, 1, 19.
[27] Kar P, Sardar S, Alarousu E, Sun J, Seddigi ZS, Ahmed SA, Danish EY, Mohammed OF, Pal SK. Impact of metal ions in porphyrin-based applied materials for visible-light photocatalysis: key information from ultrafast electronic spectroscopy. *Chem. Eur. J.* 2014, 20, 10475–10483.
[28] Seddigi ZS, Ahmed SA, Sardar S, Pal SK. Ultrafast dynamics at the zinc phthalocyanine/zinc oxide nanohybrid interface for efficient solar light harvesting in the near red region. *Sol. Energ. Mat. Sol. Cells* 2015, 143, 63–71.
[29] Kamat PV. Manipulation of charge transfer across semiconductor interface. A criterion that cannot be ignored in photocatalyst design. *J. Phys. Chem. Lett.* 2012, 3, 663–672.

[30] Kumar SG, Devi LG. Review on modified TiO_2 photocatalysis under UV/visible light: selected results and related mechanisms on interfacial charge carrier transfer dynamics. *J. Phys. Chem. A* 2011, 115, 13211–13241.
[31] Nieto-Pescador J, Abraham B, Gundlach L. Photoinduced ultrafast heterogeneous electron transfer at molecule-semiconductor interfaces. *J. Phys. Chem. Lett.* 2014, 5, 3498–3507.
[32] Tvrdy K, Frantsuzov PA, Kamat PV. Photoinduced electron transfer from semiconductor quantum dots to metal oxide nanoparticles. *Proc. Natl. Acad. Sci.* 2011, 108, 29–34.
[33] Zhou H, Fan T, Zhang D. Biotemplated materials for sustainable energy and environment: current status and challenges. *ChemSusChem.* 2011, 4, 1344–1387.
[34] Sun Y, Wu Q, Shi G. Graphene based new energy materials. *Energy Environ. Sci.* 2011, 4, 1113–1132.
[35] Peter LM. The Grätzel cell: where next? *J. Phys. Chem. Lett.* 2011, 2, 1861–1867.
[36] Robertson N. Optimizing dyes for dye-sensitized solar cells. *Angew. Chem. Int. Ed.* 2006, 45, 2338–2345.
[37] Hayashi H, Lightcap IV, Tsujimoto M, Takano M, Umeyama T, Kamat PV, Imahori H. Electron transfer cascade by organic/inorganic ternary composites of porphyrin, zinc oxide nanoparticles, and reduced graphene oxide on a tin oxide electrode that exhibits efficient photocurrent generation. *J. Am. Chem. Soc.* 2011, 133, 7684–7687.
[38] Yella A, Lee H-W, Tsao HN, Yi C, Chandiran AK, Nazeeruddin MK, Diau EW-G, Yeh C-Y, Zakeeruddin SM, Grätzel M. Porphyrin-sensitized solar cells with cobalt (II/III)-based redox electrolyte exceed 12 percent efficiency. *Science* 2011, 334, 629–634.
[39] Li L-L, Diau EW-G. Porphyrin-sensitized solar cells. *Chem. Soc. Rev.* 2013, 42, 291–304.
[40] Duan M-y, Li J, Mele G, Wang C, Lü X-F, Vasapollo G, Zhang F-X. Photocatalytic activity of novel tin porphyrin/TiO_2 based composites. *J. Phys. Chem. C* 2010, 114, 7857–7862.
[41] Sun W-j, Li J, Yao G-p, Jiang M, Zhang F-x. Efficient photodegradation of 4-nitrophenol by using new CuPp-TiO_2 photocatalyst under visible light irradiation. *Catal. Commun.* 2011, 16, 90–93.
[42] Shiragami T, Matsumoto J, Inoue H, Yasuda M. Antimony porphyrin complexes as visible-light driven photocatalyst. *J. Photochem. Photobiol. C* 2005, 6, 227–248.
[43] Sun W-j, Li J, Yao G-p, Zhang F-x, Wang J-L. Surface-modification of TiO_2 with new metalloporphyrins and their photocatalytic activity in the degradation of 4-notrophenol. *Appl. Surf. Sci.* 2011, 258, 940–945.
[44] Lu H-P, Tsai C-Y, Yen W-N, Hsieh C-P, Lee C-W, Yeh C-Y, Diau EW-G. Control of dye aggregation and electron injection for highly efficient porphyrin sensitizers adsorbed on semiconductor films with varying ratios of coadsorbate. *J. Phys. Chem. C* 2009, 113, 20990–20997.
[45] Afzal S, Daoud WA, Langford SJ. Photostable self-cleaning cotton by a copper(II) porphyrin/TiO_2 visible-light photocatalytic system. *ACS Appl. Mater. Interfaces* 2013, 5, 4753–4759.
[46] Barea EM, Gónzalez-Pedro V, Ripollés-Sanchis T, Wu H-P, Li L-L, Yeh C-Y, Diau EW-G, Bisquert J. Porphyrin dyes with high injection and low recombination for highly efficient mesoscopic dye-sensitized solar cells. *J. Phys. Chem. C* 2011, 115, 10898–10902.
[47] Panda MK, Ladomenou K, Coutsolelos AG. Porphyrins in bio-inspired transformations: light-harvesting to solar cell. *Coord. Chem. Rev.* 2012, 256, 2601–2627.
[48] Balazs AC, Emrick T, Russell TP. Nanoparticle polymer composites: where two small worlds meet. *Science* 2006, 314, 1107–1110.
[49] Ghosh S, Khan AH, Acharya S. Fabrication of highly stable, hybrid PbS nanocomposites in PAMAM dendrimer matrix for photodetection. *J. Phys. Chem. C* 2012, 116, 6022–6030.
[50] Ghosh S, Ghosh D, Bag PK, Bhattacharya SC, Saha A. Aqueous synthesis of ZnTe/dendrimer nanocomposites and their antimicrobial activity: implications in therapeutics. *Nanoscale* 2011, 3, 1139–1148.
[51] Sinha Ray S. Polylactide-based bionanocomposites: a promising class of hybrid materials. *Acc. Chem. Res.* 2012, 45, 1710–1720.
[52] Di Michele L, Zaccone A, Eiser E. Analytical theory of polymer-network-mediated interaction between colloidal particles. *Proc. Natl. Acad. Sci.* 2012, 109, 10187–10192.
[53] Wang Y, Wang Q, Zhan X, Wang F, Safdar M, He J. Visible light driven type II heterostructures and their enhanced photocatalysis properties: a review. *Nanoscale* 2013, 5, 8326–8339.
[54] Zhang N, Liu S, Xu Y-J. Recent progress on metal core@semiconductor shell nanocomposites as a promising type of photocatalyst. *Nanoscale* 2012, 4, 2227–2238.
[55] Qu Y, Duan X. Progress, challenge and perspective of heterogeneous photocatalysts. *Chem. Soc. Rev.* 2013, 42, 2568–2580.
[56] Li Q, Jin X, Yang X, Chen C, Chen Z, Qin Y, Wei T-h, Sun W. Reducing the excess energy offset in organic/inorganic hybrid solar cells: toward faster electron transfer. *Appl. Catal., B* 2015, 162, 524–531.
[57] Jin X, Sun W, Chen Z, Wei T, Chen C, He X, Yuan Y, Li Y, Li Q. Exciton generation/dissociation/charge-transfer enhancement in inorganic/organic hybrid solar cells by robust single nanocrystalline LnPxOy (Ln = Eu, Y) doping. *ACS Appl. Mater. Interfaces* 2014, 6, 8771–8781.
[58] Xing G, Mathews N, Sun S, Lim SS, Lam YM, Grätzel M, Mhaisalkar S, Sum TC. Long-range balanced electron- and hole-transport lengths in organic-inorganic $CH_3NH_3PbI_3$. *Science* 2013, 342, 344–347.
[59] Wang D, Zhang J, Luo Q, Li X, Duan Y, An J. Characterization and photocatalytic activity of poly(3-hexylthiophene)-modified TiO2 for degradation of methyl orange under visible light. *J. Hazard. Mater.* 2009, 169, 546–550.
[60] Liao G, Chen S, Quan X, Chen H, Zhang Y. Photonic crystal coupled TiO_2/polymer hybrid for efficient photocatalysis under visible light irradiation. *Environ. Sci. Technol.* 2010, 44, 3481–3485.
[61] Luo Q, Bao L, Wang D, Li X, An J. Preparation and strongly enhanced visible light photocatalytic activity of TiO_2 nanoparticles modified by conjugated derivatives of polyisoprene. *J. Phys. Chem. C* 2012, 116, 25806–25815.
[62] Wang ZL. Nanostructures of zinc oxide. *Mater. Today* 2004, 7, 26–33.
[63] Pei Z, Ding L, Lu M, Fan Z, Weng S, Hu J, Liu P. Synergistic effect in polyaniline-hybrid defective ZnO with enhanced photocatalytic activity and stability. *J. Phys. Chem. C* 2014, 118, 9570–9577.
[64] Ghosh S, Kouamé NA, Ramos L, Remita S, Dazzi A, Deniset-Besseau A, Beaunier P, Goubard F, Aubert P-H, Remita H. Conducting polymer nanostructures for photocatalysis under visible light. *Nat. Mater.* 2015, 14, 505–511.

[65] van Dijken A, Meulenkamp EA, Vanmaekelbergh D, Meijerink A. The kinetics of the radiative and nonradiative processes in nanocrystalline ZnO particles upon photoexcitation. *J. Phys. Chem. B* 2000, 104, 1715–1723.
[66] Vanheusden K, Warren WL, Seager CH, Tallant DR, Voigt JA, Gnade BE. Mechanisms behind green photoluminescence in ZnO phosphor powders. *J. Appl. Phys.* 1996, 79, 7983–7990.
[67] Lakowicz JR, *Principles of Fluorescence Spectroscopy*, 2nd ed., Kluwer Academic/Plenum: New York, 1999.
[68] Bora T, Lakshman KK, Sarkar S, Makhal A, Sardar S, Pal SK, Dutta J. Modulation of defect-mediated energy transfer from ZnO nanoparticles for the photocatalytic degradation of bilirubin. *Beilstein J. Nanotechnol.* 2013, 4, 714–725.
[69] Makhal A, Sarkar S, Bora T, Baruah S, Dutta J, Raychaudhuri AK, Pal SK. Dynamics of light harvesting in ZnO nanoparticles. *Nanotechnology* 2010, 21, 265703.
[70] Sarkar S, Sardar S, Makhal A, Dutta J, Pal S. Engineering FRET-based solar cells: manipulation of energy and electron transfer processes in a light harvesting assembly. In *High-Efficiency Solar Cells*, Wang, X, Wang, ZM, Eds., Springer International Publishing: Switzerland, 2014, pp. 267–318.
[71] Narayanan SS, Sinha SS, Pal SK. Sensitized emission from a chemotherapeutic drug conjugated to CdSe/ZnS QDs. *J. Phys. Chem. C* 2008, 112, 12716–12720.
[72] Hyun B-R, Zhong Y-W, Bartnik AC, Sun L, Abruña HD, Wise FW, Goodreau JD, Matthews JR, Leslie TM, Borrelli NF. Electron injection from colloidal PbS quantum dots into titanium dioxide nanoparticles. *ACS Nano* 2008, 2, 2206–2212.
[73] Willis SM, Cheng C, Assender HE, Watt AAR. The transitional heterojunction behavior of PbS/ZnO colloidal quantum dot solar cells. *Nano Letters* 2012, 12, 1522–1526.
[74] Plass R, Pelet S, Krueger J, Grätzel M, Bach U. Quantum dot sensitization of organic-inorganic hybrid solar cells. *J. Phys. Chem. B* 2002, 106, 7578–7580.
[75] Eichberger R, Strothkämper C, Thomas I, Hannappel T, Schwarzburg K, Fasting C, Bartelt A, Schütz R. Charge separation dynamics at inorganic/organic nanostructured hybrid photovoltaic interfaces. *J. Photon. Energy.* 2012, 2, 021003.
[76] Hoffman JB, Choi H, Kamat PV. Size-Dependent energy transfer pathways in CdSe quantum dot–squaraine light-harvesting assemblies: Förster versus Dexter. *J. Phys. Chem. C* 2014, 118, 18453–18461.
[77] Choi H, Santra PK, Kamat PV. Synchronized energy and electron transfer processes in covalently linked CdSe–squaraine dye–TiO_2 light harvesting assembly. *ACS Nano.* 2012, 6, 5718–5726.
[78] Makhal A, Sarkar S, Bora T, Baruah S, Dutta J, Raychaudhuri AK, Pal SK. Role of resonance energy transfer in light harvesting of zinc oxide-based dye-sensitized solar cells. *J. Phys. Chem. C* 2010, 114, 10390–10395.
[79] Robel I, Subramanian V, Kuno M, Kamat PV. Quantum dot solar cells. Harvesting light energy with CdSe nanocrystals molecularly linked to mesoscopic TiO_2 films. *J. Am. Chem. Soc.* 2006, 128, 2385–2393.
[80] Luther JM, Gao J, Lloyd MT, Semonin OE, Beard MC, Nozik AJ. Stability assessment on a 3% bilayer PbS/ZnO quantum dot heterojunction solar cell. *Adv. Mater.* 2010, 22, 3704–3707.
[81] Gao J, Luther JM, Semonin OE, Ellingson RJ, Nozik AJ, Beard MC. Quantum dot size dependent J-V characteristics in heterojunction ZnO/PbS quantum dot solar cells. *Nano Lett.* 2011, 11, 1002–1008.
[82] Jean J, Chang S, Brown PR, Cheng JJ, Rekemeyer PH, Bawendi MG, Gradecak S, Bulovic V. ZnO nanowire arrays for enhanced photocurrent in PbS quantum dot solar cells. *Adv. Mater.* 2013, 25, 2790–2796.
[83] Subramanian V, Wolf EE, Kamat PV. Green emission to probe photoinduced charging events in ZnO-Au nanoparticles. Charge distribution and fermi-level equilibration. *J. Phys. Chem. B* 2003, 107, 7479–7485.
[84] Subramanian V, Wolf EE, Kamat PV. Catalysis with TiO2/gold nanocomposites. Effect of metal particle size on the Fermi level equilibration. *J. Am. Chem. Soc.* 2004, 126, 4943–4950.
[85] Roy P, Periasamy AP, Liang C-T, Chang H-T. Synthesis of graphene-ZnO-Au nanocomposites for efficient photocatalytic reduction of nitrobenzene. *Environ. Sci. Technol.* 2013, 47, 6688–6695.
[86] Kim K-J, Kreider P, Chang C-H, Park C-M, Ahn H-G. Visible-light-sensitive nanoscale Au–ZnO photocatalysts. *J. Nanopart. Res.* 2013, 15, 1–11.
[87] Li P, Wei Z, Wu T, Peng Q, Li Y. Au-ZnO hybrid nanopyramids and their photocatalytic properties. *J. Am. Chem. Soc.* 2011, 133, 5660–5663.
[88] Fageria P, Gangopadhyay S, Pande S. Synthesis of ZnO/Au and ZnO/Ag nanoparticles and their photocatalytic application using UV and visible light. *RSC Adv.* 2014, 4, 24962–24972.
[89] Zhao X, Wu Y, Hao X. Electrodeposition synthesis of Au-ZnO hybrid nanowires and their photocatalytic properties. *Int. J. Electrochem. Sci.* 2013, 8, 3349–3356.
[90] Chen Y, Zeng D, Zhang K, Lu A, Wang L, Peng D-L. Au-ZnO hybrid nanoflowers, nanomultipods and nanopyramids: one-pot reaction synthesis and photocatalytic properties. *Nanoscale* 2014, 6, 874–881.
[91] Fragua DM, Abargues R, Rodriguez-Canto PJ, Sanchez-Royo JF, Agouram S, Martinez-Pastor JP. Au–ZnO nanocomposite films for plasmonic photocatalysis. *Adv. Mater. Interfaces* 2015, 2, 1500156 (1–10).
[92] Castillero P, Sánchez-Valencia JR, Cano M, Pedrosa JM, Roales J, Barranco A, González-Elipe AnR. Active and optically transparent tetracationic porphyrin/TiO_2 composite thin films. *ACS Appl. Mater. Interfaces* 2010, 2, 712–721.
[93] Huang H, Gu X, Zhou J, Ji K, Liu H, Feng Y. Photocatalytic degradation of Rhodamine B on TiO_2 nanoparticles modified with porphyrin and iron-porphyrin. *Catal. Commun.* 2009, 11, 58–61.
[94] Kruglik SG, Apanasevich PA, Chirvony VS, Kvach VV, Orlovich VA. Resonance Raman, CARS, and picosecond absorption spectroscopy of copper porphyrins: the evidence for the Exciplex formation with oxygen-containing solvent molecules. *J. Phys. Chem.* 1995, 99, 2978–2995.
[95] Dabrowski JM, Pucelik B, Pereira MM, Arnaut LG, Macyk W, Stochel G. New hybrid materials based on halogenated metalloporphyrins for enhanced visible light photocatalysis. *RSC Adv.* 2015, 5, 93252–93261.
[96] Radivojevic I, Bazzan G, Burton-Pye BP, Ithisuphalap K, Saleh R, Durstock MF, Francesconi LC, Drain CM. Zirconium(IV) and hafnium(IV) porphyrin and phthalocyanine complexes as new dyes for solar cell devices. *J. Phys. Chem. C* 2012, 116, 15867–15877.
[97] Imahori H, Kang S, Hayashi H, Haruta M, Kurata H, Isoda S, Canton SE, Infahsaeng Y, Kathiravan A, Pascher T, Chabera P, Yartsev AP, Sundstrom V. Photoinduced charge carrier

dynamics of Zn-porphyrin-TiO_2 electrodes: the key role of charge recombination for solar cell performance. *J. Phys. Chem. A* 2011, 115, 3679–3690.
[98] Brédas J-L, Cornil J, Beljonne D, dos Santos DA, Shuai Z. Excited-state electronic structure of conjugated oligomers and polymers: a quantum-chemical approach to optical phenomena. *Acc. Chem. Res.* 1999, 32, 267–276.
[99] Liu R. Hybrid organic/inorganic nanocomposites for photovoltaic cells. *Materials* 2014, 7, 2747–2771.
[100] Ghosh S, Priyam A, Bhattacharya S, Saha A. Mechanistic aspects of quantum dot based probing of Cu (II) ions: role of dendrimer in sensor efficiency. *J Fluoresc* 2009, 19, 723–731.
[101] Martin ST, Lee AT, Hoffmann MR. Chemical mechanism of inorganic oxidants in the TiO2/UV process: increased rates of degradation of chlorinated hydrocarbons. *Environ. Sci. Technol.* 1995, 29, 2567–2573.
[102] Su Y-W, Lin W-H, Hsu Y-J, Wei K-H. Conjugated polymer/nanocrystal nanocomposites for renewable energy applications in photovoltaics and photocatalysis. *Small* 2014, 10, 4427–4442.
[103] Kango S, Kalia S, Celli A, Njuguna J, Habibi Y, Kumar R. Surface modification of inorganic nanoparticles for development of organic–inorganic nanocomposites – a review. *Prog. Polym. Sci.* 2013, 38, 1232–1261.
[104] Abdiryim T, Ali A, Jamal R, Osman Y, Zhang Y. A facile solid-state heating method for preparation of poly(3,4-ethelenedioxythiophene)/ZnO nanocomposite and photocatalytic activity. *Nanoscale Res. Lett.* 2014, 9, 1–8.

Bionotes

Samim Sardar
Department of Chemical, Biological and Macromolecular Sciences, S. N. Bose National Centre for Basic Sciences, Block JD, Sector III, Salt Lake City, Kolkata 700 098, India

Samim Sardar received his BSc (2010, University of Calcutta, India) and MSc (2012, IIT Delhi, India) degrees in Chemistry. He is currently pursuing his PhD under the supervision of Professor Samir Kumar Pal at the S N Bose National Centre for Basic Sciences, Kolkata, India. The focus of his study is to explore the fundamental ultrafast (femtosecond and picosecond) processes at the heterogeneous interfaces for potential light-harvesting applications.

Samir Kumar Pal
Department of Chemical, Biological and Macromolecular Sciences, S. N. Bose National Centre for Basic Sciences, Block JD, Sector III, Salt Lake City, Kolkata 700 098, India,
skpal@bose.res.in

Samir Kumar Pal received his PhD (2000) from Jadavpur University. After completion of his PhD, he joined the research group of Professor Ahmed H. Zewail at the California Institute of Technology. Currently, he is a Professor in the Department of Chemical, Biological and Macromolecular Sciences, S N Bose National Centre for Basic Sciences, Kolkata, India. His current research interests center on the ultrafast spectroscopy of molecules and nanomaterials, solar devices, and biomedical instrumentation.